

Iron Force Constants of Bridgmanite at High Pressure: Implications for Iron Isotope Fractionation in the Deep Mantle

Wenzhong Wang^{1,2*}, Jiachao Liu^{3,4}, Hong Yang^{5†}, Susannah M. Dorfman^{4,*}, Mingda Lv⁴, Jie Li⁶, Feng Zhu⁶, Jiyong Zhao⁷, Michael Y. Hu⁷, Wenli Bi^{7,8}, Ercan E. Alp⁷, Yuming Xiao⁹, Zhongqing Wu^{1,*}, Jung-Fu Lin^{3,*}

¹Laboratory of Seismology and Physics of Earth's Interior, School of Earth and Space Sciences, University of Science and Technology of China, Hefei, China;

²Department of Earth Sciences, University College London, Gower Street, London WC1E 6BT, UK;

³Department of Geological Sciences, Jackson School of Geosciences, The University of Texas at Austin, Austin, Texas 78712, USA;

⁴Department of Earth and Environmental Sciences, Michigan State University, MI 48824, USA

⁵Center for High Pressure Science and Technology Advanced Research (HPSTAR), Pudong, Shanghai 201203, China;

⁶Department of Earth and Environmental Sciences, University of Michigan, MI 48109, USA;

⁷Advanced Photon Source, Argonne National Laboratory, Argonne, Illinois 60439, USA;

⁸Department of Geology, University of Illinois at Urbana-Champaign, Urbana, Illinois 61801, USA;

⁹High Pressure Collaborative Access Team (HPCAT), X-Ray Science Division, Argonne National Lab, Argonne, Illinois 60439, USA;

† Now at Department of Geological Sciences, Stanford University, Stanford, CA 94305, USA.

* J.C. Liu and W.Z. Wang contributed equally to this work.

Corresponding authors: W. Wang (wenzhong.wang@ucl.ac.uk), S. M. Dorfman (dorfman3@msu.edu), J.F. Lin (afu@jsg.utexas.edu), or Zhongqing Wu (wuzq10@ustc.edu.cn)

1 **Abstract**

2 The isotopic compositions of iron in major mantle minerals may record chemical
3 exchange between deep-Earth reservoirs as a result of early differentiation and ongoing
4 plate tectonics processes. Bridgmanite (Bdg), the most abundant mineral in the Earth's
5 lower mantle, can incorporate not only Al but also Fe with different oxidation states
6 and spin states, which in turn can influence the distribution of Fe isotopes between Bdg
7 and ferropericlasite (Fp) and between the lower mantle and the core. In this study, we
8 combined first-principles calculations with high-pressure nuclear resonant inelastic X-
9 ray scattering measurements to evaluate the effects of Fe site occupancy, valence, and
10 spin states at lower-mantle conditions on the reduced Fe partition function ratio (β -
11 factor) of Bdg. Our results show that the spin transition of octahedral-site (B-site) Fe³⁺
12 in Bdg under mid-lower-mantle conditions generates a +0.09‰ increase in its β -factor,
13 which is the most significant effect compared to Fe site occupancy and valence. Fe²⁺-
14 bearing Bdg varieties have smaller β -factor relative to Fe³⁺-bearing varieties, especially
15 those containing B-site Fe³⁺. Our models suggest that Fe isotopic fractionation between
16 Bdg and Fp is only significant in the lowermost mantle due to the occurrence of low-
17 spin Fe²⁺ in Fp. Assuming early segregation of an iron core from a deep magma ocean,
18 we find that neither core formation nor magma ocean crystallization would have
19 resulted in resolvable Fe isotope fractionation. In contrast, Fe isotopic fractionation
20 between low-spin Fe³⁺-bearing Bdg/Fe²⁺-bearing Fp and metallic iron at the core-
21 mantle boundary may have enriched the lowermost mantle in heavy Fe isotopes by up
22 to +0.20‰.

23 **Keywords:** Fe isotopic fractionation, bridgmanite, spin transition, nuclear resonant
24 spectroscopy, first-principles calculations

25

26 **1. Introduction**

27 Iron, the most abundant element in the Earth by weight, is the dominant component
28 of the core and the only major transition metal in the mantle. Signatures of planetary
29 accretion and differentiation may be recorded in the Fe isotopic compositions
30 ($\delta^i\text{Fe} = ((^i\text{Fe}/^{54}\text{Fe})_{\text{sample}} / (^i\text{Fe}/^{54}\text{Fe})_{\text{standard}} - 1) * 1000 \text{ ‰}$, $i=56$ or 57) in the Earth's crust,
31 mantle, and core (Poitrasson et al., 2009; Polyakov, 2009; Poitrasson et al., 2013; Rubie

32 et al., 2015; Sossi et al., 2016; Elardo and Shahar, 2017; Teng et al., 2017). Terrestrial
33 mid-ocean ridge basalts (MORBs) exhibit strikingly high $\delta^{56}\text{Fe}$ of $0.105 \pm 0.006\%$
34 (Teng et al., 2013) relative to chondritic values, suggesting the enrichment of heavy Fe
35 isotopes in the Earth's upper mantle. Several hypotheses have been proposed to explain
36 the Fe isotope signatures in the mantle, including evaporation loss of light iron isotopes
37 during Earth's accretion (Poitrasson et al., 2004; Poitrasson, 2007), Fe isotopic
38 fractionation during core formation (Polyakov, 2009; Elardo and Shahar, 2017), and
39 mantle partial melting (Teng et al., 2008; Dauphas et al., 2014). Evaluation of the effects
40 of these processes on the Fe isotope composition requires Fe equilibrium isotopic
41 fractionation factors ($\Delta^{56}\text{Fe}$) between major Fe-bearing mantle and core minerals/melts
42 under pressure-temperature (P-T) conditions relevant to the early and current Earth's
43 interior.

44 Bridgmanite (Bdg) and ferropericlaase (Fp) are the most abundant Fe-bearing
45 minerals in the lower mantle. As such, the reduced Fe partition function ratios (β -factors)
46 for Bdg, Fp, and iron-light element alloys are key parameters for modelling Fe isotopic
47 fractionation between different minerals/melts in the lower mantle or between the
48 mantle and the core. Generally, β -factors are directly controlled by bond stiffnesses in
49 structures, which in turn depend on structural response to pressure, temperature, and
50 composition (Schauble, 2011; Huang et al., 2013; Huang et al., 2014; Wu et al., 2015a;
51 Shahar et al., 2016; Liu et al., 2017; Yang et al., 2019). In addition, Fe in both Bdg and
52 Fp have been found to undergo spin transitions under mid-lower-mantle conditions (e.g.,
53 Lin et al., 2013; Liu et al., 2018), which can significantly change their electronic
54 structures (Hsu et al., 2011), Fe bond stiffnesses (Polyakov, 2009; Rustad and Yin, 2009;
55 Lin et al., 2013), and hence presumably influence Fe isotope fractionation. A recent
56 work conducted by Yang et al. (2019) observed a significant increase in the β -factor of
57 Fp across its Fe^{2+} spin transition in the octahedral site at ~ 60 GPa and 300 K, whereas
58 the β -factor of Bdg remains unchanged with increasing pressure likely due to lattice
59 distortion. Additionally, the effects of light elements on the β -factor of metallic Fe alloy
60 at high P-T conditions will also affect our understanding of deep-Earth iron isotope
61 distribution (Chen et al., 2014; Shahar et al., 2016; Liu et al., 2017; Chen et al., 2018).

62 The pressure-dependence of the β -factor of Bdg can be very complex when

63 considering the two possible crystallographic sites can accommodate Fe with different
64 valences and spin states as well as other minor cations like Al. The individual
65 contribution of each lattice site to the mean force constant of the phase cannot be
66 uniquely determined in high-pressure nuclear resonant inelastic X-ray scattering
67 measurements (e.g., Yang et al. 2019) which yields only the total average inelastic
68 scattering behavior of the sample. The Bdg structure accommodates Fe in both the
69 larger pseudo-dodecahedral (8-fold) A-site and the smaller octahedral (6-fold) B-site
70 (Lin et al., 2013). While Fe^{2+} can only reside in the large A-site, Fe^{3+} can enter both
71 sites through different proposed substitution mechanisms such as $\text{Mg}^{2+}_{\text{A}} + \text{Si}^{4+}_{\text{B}} \rightarrow$
72 $\text{Fe}^{3+}_{\text{A}} + \text{Fe}^{3+}_{\text{B}}$ and $\text{Mg}^{2+}_{\text{A}} + \text{Si}^{4+}_{\text{B}} \rightarrow \text{Fe}^{3+}_{\text{A}} + \text{Al}^{3+}_{\text{B}}$ (Frost et al., 2004; Liu et al., 2015). Only
73 Fe^{3+} in the Bdg B-site is expected to undergo a high-spin (HS) to low-spin (LS)
74 transition at pressures corresponding to mid-mantle depths, while A-site Fe^{2+} and Fe^{3+}
75 experience lattice distortion but both valence states maintain HS state throughout the
76 lower mantle (Catalli et al., 2010; Hsu et al., 2011; Mao et al., 2015; Shukla and
77 Wentzcovitch, 2016; Fu et al., 2018b; Liu et al., 2018).

78 Many previous studies have argued that iron exists predominantly as Fe^{3+} in Bdg,
79 on the basis of increased stability of Fe^{3+} in Bdg structure at lower-mantle-relevant
80 oxygen fugacity conditions (Catalli et al., 2010; Frost et al., 2004; Frost and
81 McCammon, 2008; Li et al., 2006; Marquardt et al., 2009; McCammon, 1997).
82 Furthermore, a recent work (Armstrong et al., 2019) also found that Fe^{2+} in a deep
83 magma ocean would disproportionate to Fe^{3+} plus metallic iron at high pressures. As
84 such, consequent segregation of precipitated iron metal from the lower mantle into the
85 core could leave the Bdg enriched in Fe^{3+} after magma ocean crystallization. In addition,
86 experimental studies (Frost et al., 2004; Shim et al., 2017; Andrault et al., 2018) also
87 reported Fe^{3+} -rich Bdg in equilibrium with iron metal due to the disproportionation of
88 Fe^{2+} . Although recent experimental and theoretical studies have reported the β -factors
89 of several Bdg compositions (Shahar et al., 2016; Yang et al., 2019), none of the studies
90 have examined the effect of Fe^{3+} in the B-site, precluding the evaluation of the influence
91 of the B-site Fe^{3+} spin transition on the β -factors of Bdg. In addition to Fe^{3+} , Al^{3+} can
92 also enter A and B sites in Bdg through the coupled substitution mechanism $\text{Mg}^{2+}_{\text{A}} +$
93 $\text{Si}^{4+}_{\text{B}} = (\text{Fe}^{3+}, \text{Al}^{3+})_{\text{A}} + (\text{Fe}^{3+}, \text{Al}^{3+})_{\text{B}}$ (Frost et al., 2004; Liu et al., 2015; Shim et al.,

94 2017; Yang et al., 2019). As the radius of Al^{3+} is smaller than both A-site and B-site
95 Fe^{3+} , it prefers to substitute into the smaller B-site and the content of B-site Fe^{3+} is
96 influenced by the Fe^{3+}/Al ratio (Frost et al., 2004; Liu et al., 2015; Shim et al., 2017).
97 Thus, comparison of the β -factors between Al-bearing and Al-free Bdg is needed to
98 reveal the effect of Al on the β -factor of Bdg.

99 In this study, we determine the β -factors of $(\text{Mg}_{0.5}\text{Fe}^{3+}_{0.5})(\text{Si}_{0.5}\text{Fe}^{3+}_{0.5})\text{O}_3$ Bdg at
100 mantle-relevant pressures by both nuclear resonant inelastic X-ray scattering (NRIXS)
101 and the density functional theory (DFT) augmented by a Hubbard U correction method.
102 The spin transition of the B-site Fe^{3+} in $(\text{Mg}_{0.5}\text{Fe}^{3+}_{0.5})(\text{Si}_{0.5}\text{Fe}^{3+}_{0.5})\text{O}_3$ Bdg at 43-50 GPa
103 has been inferred from X-ray diffraction, X-ray emission and electrical conductivity
104 measurements (Liu et al., 2018). This sample thus offers the possibility to
105 unambiguously determine the influence of the B-site Fe^{3+} spin transition on its β -factor.
106 In addition, the pressure- and temperature-dependent β -factors of Fe in four other
107 bridgmanite compositions were calculated by the DFT+ U method, including Fe^{3+} - and
108 Al^{3+} -bearing Bdg, $(\text{Mg}_{0.9375}\text{Fe}^{3+}_{0.0625})(\text{Si}_{0.9375}\text{Al}_{0.0625})\text{O}_3$, $(\text{Mg}_{0.75}\text{Fe}^{3+}_{0.25})(\text{Si}_{0.75}\text{Al}_{0.25})\text{O}_3$,
109 and Fe^{2+} -bearing Bdg, $(\text{Mg}_{0.75}\text{Fe}^{2+}_{0.25})\text{SiO}_3$ and $(\text{Mg}_{0.5}\text{Fe}^{2+}_{0.5})\text{SiO}_3$. The calculated
110 results are used to constrain the effects of valence, spin states, and site occupancies of
111 Fe in Bdg on its β -factor at high pressure and temperature. To assess how Fe isotopes
112 distribute between Bdg and Fp in the lower mantle, our results are further used to model
113 the depth-dependence of $\Delta^{56}\text{Fe}_{\text{Bdg-Fp}}$ for various bulk mantle compositions. Finally, we
114 estimate the effect of Fe species in Bdg, Fp, and metallic iron-light element alloys on
115 the scale of Fe isotopic fractionation between the lower mantle and the core.

116

117 **2. Materials and Methods**

118 **2.1. Bridgmanite sample synthesis and DAC preparation**

119 ^{57}Fe -enriched $(\text{Mg}_{0.46}\text{Fe}^{3+}_{0.53})(\text{Si}_{0.49}\text{Fe}^{3+}_{0.51})\text{O}_3$ Bdg sample was synthesized as in
120 Liu et al. (2018). Briefly, fine-powdered 94.45% ^{57}Fe -enriched Fe_2O_3 (Cambridge
121 Isotope Laboratories) was homogeneously mixed with MgO and SiO_2 in 1:1:1 molar
122 ratios. $(\text{Mg}_{0.46}\text{Fe}^{3+}_{0.53})(\text{Si}_{0.49}\text{Fe}^{3+}_{0.51})\text{O}_3$ akimotoite was recovered from the multi-anvil
123 synthesis at 24 GPa and 1873 K for ~ 9 hours. The sample used in this study is from
124 the same multi-anvil press synthesis used in Liu et al. (2018) and (Dorfman et al. (2020)).

125 Multiple experimental runs confirmed via refinement of X-ray diffraction data that this
126 akimotoite reproducibly and reversibly transforms to Bdg at ~ 24 GPa and 300 K
127 (Dorfman et al. 2018), therefore the NRIXS measurements collected at 32.5 GPa and
128 above are within the stability field of Bdg. Synchrotron Mössbauer spectroscopy (Liu
129 et al., 2018) and conventional Mössbauer spectroscopy (Dorfman et al., 2020) confirm
130 that all Fe in this sample is Fe^{3+} , which enters Bdg structure through coupled
131 substitution ($\text{Mg}^{2+}_{\text{A}} + \text{Si}^{4+}_{\text{B}} = \text{Fe}^{3+}_{\text{A}} + \text{Fe}^{3+}_{\text{B}}$).

132 A panoramic diamond anvil cell (DAC) equipped with a pair of 300- μm culet
133 diamonds was used for NRIXS measurements up to 60.9 GPa. NRIXS signals at higher
134 pressures were measured from a three-opening panoramic DAC equipped with a pair
135 of 150- μm culet diamonds and three APD detectors at Argonne National Laboratory.
136 To increase the signal-to-background ratio, the upstream diamond was partially
137 perforated to reduce scattering of the incoming X-ray beam. X-ray transparent, high-
138 purity Be gaskets 3 mm in diameter with cubic boron nitride (c-BN) inserts were used
139 to support sample chamber and provide windows for NRIXS signal collection. The c-
140 BN insert was preindented to ~ 30 - μm thickness before a ~ 70 - μm -diameter sample
141 chamber was drilled on its center. In the sample chamber, $\sim 15 \times 15 \times 10 \mu\text{m}^3$ sample was
142 sandwiched between two layers of ~ 5 - μm -thick NaCl pressure medium. 5- μm ruby
143 spheres next to the samples were used as pressure gauge (Mao et al., 1986) below ~ 70
144 GPa. For higher pressure experiments, pressures were determined from the edge of the
145 diamond Raman peak measured at the sample position (Akahama and Kawamura,
146 2010).

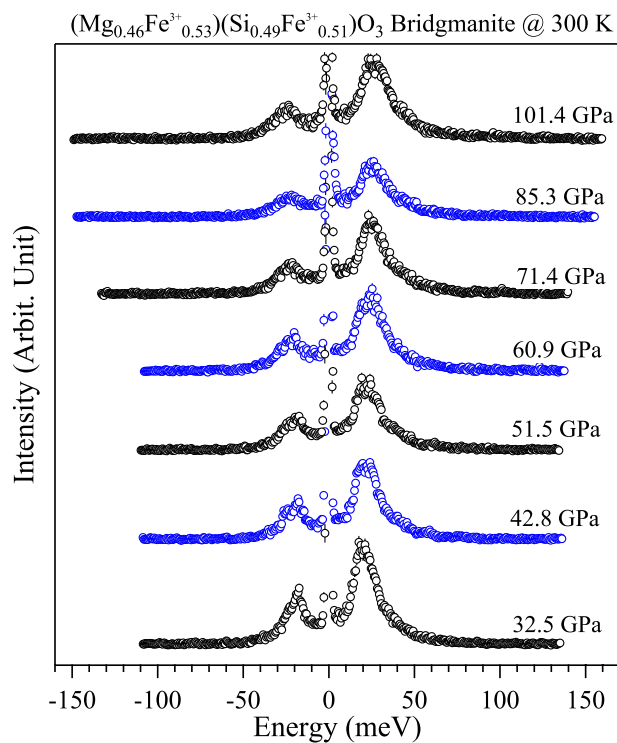
147

148 **2.2. NRIXS measurements and data analysis**

149 NRIXS measurements for ^{57}Fe -enriched $(\text{Mg}_{0.46}\text{Fe}^{3+}_{0.53})(\text{Si}_{0.49}\text{Fe}^{3+}_{0.51})\text{O}_3$ Bdg
150 sample (Fig. 1) at 32.5-60.9 GPa and 71.4-101.4 GPa were conducted at beamlines 16-
151 ID-D and 3-ID-B of the Advanced Photon Source, Argonne National Laboratory,
152 respectively. At both beamlines the incident X-ray beam was focused to $\sim 10 \mu\text{m}$ in
153 diameter on the sample in a DAC. NRIXS spectra were collected by avalanche photo
154 diode (APD) detectors attached to DACs, respectively. Each NRIXS spectrum was
155 generated by scanning energy near the ^{57}Fe nuclear transition energy of 14.4125 keV

156 by tuning a high-resolution monochromator. The energy resolution was 1 meV with a
157 step size of 0.334 meV at beamline 3-IDB and 2 meV with a step size of 0.67 meV at
158 beamline 16-ID-D. Collection times were 3-5 s/step, for a total of ~1 hour per NRIXS
159 spectrum. At each pressure, 15-40 NRIXS spectra were collected and summed to make
160 sufficient signal-to-noise ratio (Fig. 1). The spectra at pressure below 60.9 GPa were
161 collected at 16 IDD while others were collected at 3-ID-B. The ranges of scanned
162 energy for each spectrum can be found in Fig. 1. These wide energy ranges are critical
163 for capturing the multi-phonon contributions to PDOS and reliable background removal
164 (Dauphas et al., 2018).

165 NRIXS data were processed using the software package *SciPhon* (Dauphas et al.,
166 2018). First the energy resolution function of the incident X-ray was used to
167 deconvolute the NRIXS spectrum and a linear background based on high-energy
168 (beyond ± 100 meV) part of the spectrum was subtracted. The NRIXS spectrum was
169 then used to derive the phonon density of states (PDOS) of iron atoms in the lattice.
170 This derivation uses the harmonic approximation, which assumes the lattice potentials
171 are proportional to atomic displacement squared.



172

173 **Figure 1.** NRIXS spectra of ⁵⁷Fe-enriched (Mg_{0.5}Fe³⁺_{0.5})(Si_{0.5}Fe³⁺_{0.5})O₃ bridgmanite sample at
174 300 K and high pressures. The peak at 0 meV corresponds to the recoilless elastic scattering,

175 while the other inelastic peaks origin from either phonon creation ($E > 0$) or annihilation ($E <$
176 0).

177

178 **2.3. First-principles calculations**

179 All calculations were performed using the Quantum Espresso package (Giannozzi
180 et al., 2009) based on density functional theory (DFT), plane wave, and pseudopotential.
181 The local density approximation (LDA) was adopted for the exchange correlation
182 function. The energy cutoff for plane waves was 70 Ry. The pseudopotentials for Mg,
183 Si, O, and Al were well described in our previous studies (Huang et al., 2013; Huang et
184 al., 2014; Wu et al., 2015a; Wang and Wu, 2018). The pseudopotential for Fe was
185 generated using the Vanderbilt method (Vanderbilt, 1990) with a valence configuration
186 of $3s^23p^63d^{6.5}4s^14p^0$ and a cutoff radius of 1.8 Bohr. These pseudopotentials have been
187 successfully applied to predict the structures, vibrational properties, elasticity, and
188 equilibrium isotope fractionation of mantle silicate minerals including bridgmanite in
189 our previous studies (Núñez Valdez et al., 2012; Núñez-Valdez et al., 2013; Huang et
190 al., 2013; Huang et al., 2014; Feng et al., 2014; Wu et al., 2015b; Shukla et al., 2015;
191 Wang et al., 2017a; Wang et al., 2017b; Qian et al., 2018; Wang et al., 2019a). To
192 address the large on-site Coulomb interactions among the localized electrons (Fe 3d
193 electrons) (Anisimov et al., 1991), we introduced a Hubbard U correction to the LDA
194 (LDA+ U) for all DFT calculations. U values for Fe^{2+} and Fe^{3+} on A- and/or B- sites in
195 bridgmanite are obtained from previous work (Hsu et al., 2010; Hsu et al., 2011), in
196 which values were non-empirically determined using linear response method
197 (Cococcioni and de Gironcoli, 2005). The U values for A-site Fe^{2+} , A-site HS Fe^{3+} , B-
198 site HS Fe^{3+} , B-site LS Fe^{3+} are 3.1 eV, 3.7 eV, 3.3 eV, and 4.9 eV, respectively. The
199 LDA+ U method has been widely and successfully applied to predict the physical and
200 chemical properties of Fe-bearing Bdg and Fp (Hsu et al., 2011; Wu et al., 2013; Shukla
201 and Wentzcovitch, 2016). For $(Mg_{0.5}Fe^{3+}_{0.5})(Si_{0.5}Fe^{3+}_{0.5})O_3$
202 $(Mg_{0.9375}Fe^{3+}_{0.0625})(Si_{0.9375}Al_{0.0625})O_3$, and $(Mg_{0.75}Fe^{3+}_{0.25})(Si_{0.75}Al_{0.25})O_3$ Bdg, we
203 consider only configurations with the nearest neighbor $[Fe^{3+}]_{Mg}-[Fe^{3+}/Al^{3+}]_{Si}$ since they
204 are the lowest energy configurations (Hsu et al., 2011; Shukla and Wentzcovitch, 2016).
205 Crystal structures at variable pressures were optimized on a $6 \times 6 \times 4$ k-point mesh, and

206 vibrational density of states (VDOS) were calculated using the finite displacement
 207 method as implemented in the code PHONOPYT (Togo and Tanaka, 2015). At static
 208 conditions, the B-site Fe³⁺ undergoes a HS-LS transition at ~52 GPa, consistent with
 209 previous LDA+U calculations (Shukla and Wentzcovitch, 2016). This value is ~8 GPa
 210 larger than the spin-transition pressure in (Mg_{0.875}Fe³⁺_{0.125})(Si_{0.875}Fe³⁺_{0.125})O₃ Bdg due
 211 to the difference in Fe³⁺ content.

212 Reduced partition function ratios were computed from phonon frequencies
 213 obtained from DFT calculations. The reduced partition function ratio β_A of the element
 214 X in phase A, which represents the equilibrium isotope fractionation factor between the
 215 phase A and an ideal gas of X atoms, can be expressed within the quasi-harmonic
 216 approximation as:

$$217 \quad \beta_A = \frac{Q_h}{Q_l} = \prod_i^{3N} \frac{u_{ih}}{u_{il}} \frac{e^{-\frac{1}{2}u_{ih}}}{1-e^{-u_{ih}}} \frac{1-e^{-u_{il}}}{e^{-\frac{1}{2}u_{il}}} \quad (1)$$

218 where h and l refer to the heavy and light isotopes respectively; i is a running index for
 219 the vibrational frequency, and N is the number of atoms in the unit cell. Q_h and Q_l
 220 represent the vibrational partition function for the heavy and light isotopes, respectively.
 221 Parameters u_{ih} and u_{il} are defined as:

$$222 \quad u_{ih \text{ or } il} = \hbar\omega_{ih \text{ or } il}/k_B T \quad (2)$$

223 Parameters \hbar and k_B are the reduced Planck and Boltzmann constants, respectively;
 224 T is temperature in Kelvin, and $\omega_{ih \text{ or } il}$ is the vibrational frequency of the i^{th} mode.

225 Notably, β in Eq. (1) is volume-dependent as phonon frequencies from the DFT+U
 226 calculations are a function of volume. In order to express β as a function of pressure (P)
 227 and temperature (T), we calculated the equation of state $V(P, T)$ from the Helmholtz
 228 free energy, which can be written within the quasi-harmonic approximation as:

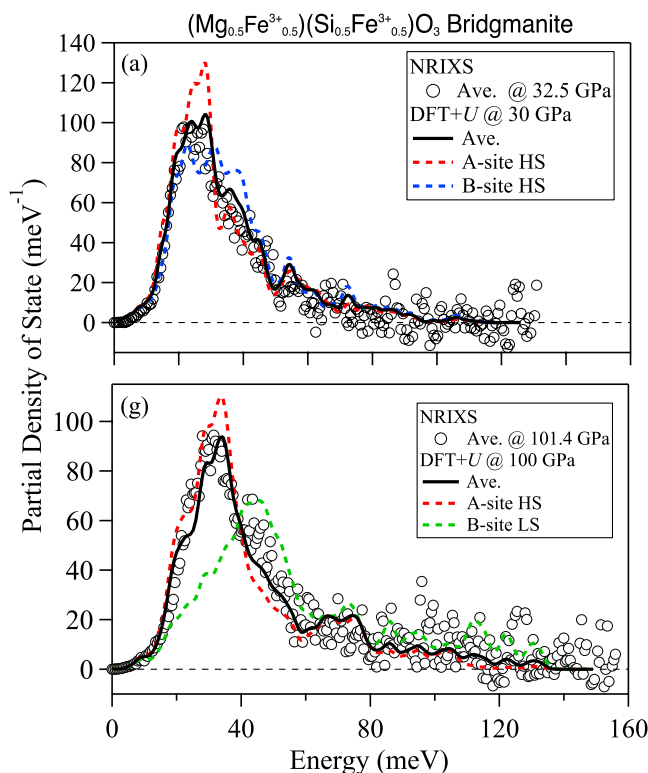
$$229 \quad F(V, T) = U(V) + \frac{1}{2} \sum_{q,m} \hbar\omega_{q,m}(V) + k_B T \sum_{q,m} \ln \left(1 - \exp \left(-\frac{\hbar\omega_{q,m}(V)}{k_B T} \right) \right) \quad (3)$$

230 where q is a wave vector in the Brillouin zone and m is a running index of phonon mode.
 231 The first, second, and third terms in Eq. (3) correspond to the static, zero-point, and
 232 vibrational energy contributions, respectively. The calculated Helmholtz free energy
 233 versus volume was fitted by the third-order Birch–Murnaghan finite strain equation of
 234 state. Consequently, the pressure- and temperature-dependent β can be derived and the
 235 equilibrium isotope fractionation factor between two Phases A and B can be obtained

236 in per mil (‰) as:

237
$$\Delta_{A-B} \approx 10^3 \ln \alpha_{A-B} = 10^3 \ln \beta_A - 10^3 \ln \beta_B \quad (4)$$

238



239

240 **Figure 2.** Representative partial phonon density of states (PDOS) of Fe³⁺ in
241 (Mg_{0.5}Fe³⁺_{0.5})(Si_{0.5}Fe³⁺_{0.5})O₃ bridgmanite derived from both NRIXS measurements and DFT+U
242 calculations. The open circles are the averaged PDOS of all Fe ions in the Bdg measured by
243 NRIXS; (a): 32.5 GPa, (b): 101.4 GPa. The blue dotted, red dashed, and green dashed curves
244 are the PDOS of A-site HS Fe³⁺, B-site HS Fe³⁺ and B-site LS Fe³⁺ from DFT+U calculations,
245 respectively. The black curves represent best-fit linear mixing model between DFT+U
246 calculated PDOS of the A-site and B-site Fe³⁺. The best-fit ratio of the weights is 50:50 for A-
247 site and B-site HS Fe³⁺ PDOS in (a); the ratio changes to 70:30 for A-site HS and B-site LS
248 Fe³⁺ PODS in (b).

249

250 3. Results

251 3.1 Partial phonon density of state of Fe in bridgmanite

252 For all pressures investigated, the calculated PDOS of Fe agree well with
253 experimental PDOS (Fig. 2 and S1). Theoretical calculations provide the PDOS of the
254 A-site and B-site Fe³⁺ individually, while the PDOS of Fe in

255 (Mg_{0.5}Fe³⁺_{0.5})(Si_{0.5}Fe³⁺_{0.5})O₃ Bdg derived from NRIXS measurements is a sum of
 256 contributions from both A-site and B-site Fe³⁺. Comparisons between experimental
 257 observations of the PDOS, predictions for individual sites, and best-fit weighted
 258 average of calculated PDOS are shown for two representative pressures (Fig. 2). In
 259 theory, the ratio of A-site and B-site Fe³⁺ contributions to the final PDOS is the
 260 concentration ratio, 50:50. At ~30 GPa, the dominant peaks in the predicted PDOS of
 261 the A-site and B-site HS Fe³⁺ are located at ~17-31 meV and 17-43 meV, respectively
 262 (Fig. 2a). A 50-50 average of these calculated PDOS for A-site HS Fe³⁺ and B-site HS
 263 Fe³⁺ by DFT+*U* matches well with the experimental PDOS (Fig. 2a). This is in good
 264 agreement with the X-ray emission spectroscopy analysis that Bdg is 100% HS at this
 265 pressure (Liu et al., 2018). At ~100 GPa, DFT+*U* calculations indicate that the
 266 transition of B-site HS Fe³⁺ to LS state significantly change the PDOS: compared with
 267 the B-site HS Fe³⁺, the predicted PDOS of the B-site LS Fe³⁺ is narrower and the
 268 dominant peaks are located at higher energies by ~11.7 meV (Fig. 2b). Accordingly,
 269 NRIXS observations demonstrate a shift of the major peak to higher energy, from ~25
 270 meV at 30 GPa to ~30 meV at 100 GPa, and an increase in intensity at ~45 meV due to
 271 this B-site LS Fe³⁺ component. In order to match experimentally derived PDOS, the
 272 best weights of the calculated PDOS of A-site HS Fe³⁺ and B-site LS Fe³⁺ are 70:30
 273 (Fig. 2b). This difference in weight ratio implies that the inelastic component of B-site
 274 LS Fe³⁺ from NRIXS measurements is significantly reduced across the spin transition.
 275 This is also consistent with the pressure dependence of the Lamb-Mössbauer factor (*f*)
 276 derived from NRIXS spectra (Fig. S2), which is directly controlled by the inelastic
 277 component (*S_{inelastic}*) in the NRIXS spectra (Dauphas et al., 2018):

$$278 \quad f_{\text{LM}} = 1 - \int_{E_{\text{min}}}^{E_{\text{max}}} S_{\text{inelastic}}(E) dE \quad (5)$$

279 Across the spin transition of B-site Fe³⁺ in (Mg_{0.5}Fe³⁺_{0.5})(Si_{0.5}Fe³⁺_{0.5})O₃ Bdg, the linear
 280 slope of *f_{LM}* with respect to pressure increases from 6.7e⁻⁴ GPa⁻¹ at 25-60 GPa to 1.6e⁻³
 281 GPa⁻¹ at ~60-70 GPa and changes to 3.7e⁻⁴ GPa⁻¹ above ~70 GPa. Accounting for the
 282 change in the inelastic scattering profile of LS Fe³⁺, NRIXS experiments and DFT+*U*
 283 calculation agree with complementary X-ray diffraction and X-ray emission
 284 spectroscopy observations about the conditions of the spin transition in Bdg.

285

286 3.2 Force constant of Fe and β -factors of $^{56}\text{Fe}/^{54}\text{Fe}$ for bridgmanite

287 From experimental and theoretical PDOS, the force constant of iron $\langle F \rangle$ and the
288 β -factors of $^{56}\text{Fe}/^{54}\text{Fe}$ for $(\text{Mg}_{0.5}\text{Fe}^{3+}_{0.5})(\text{Si}_{0.5}\text{Fe}^{3+}_{0.5})\text{O}_3$ Bdg can be obtained within the
289 harmonic approximation by following Eq. (6) and Eq. (7) (Dauphas et al., 2012):

$$290 \quad \langle F \rangle = \frac{M}{\hbar^2} \int_0^{+\infty} E^2 g(E) dE \quad (6)$$

$$291 \quad 10^3 \ln \beta = 1000 \left(\frac{1}{M^{54}\text{Fe}} - \frac{1}{M^{56}\text{Fe}} \right) \frac{\hbar^2}{8k^2 T^2} \langle F \rangle \quad (7)$$

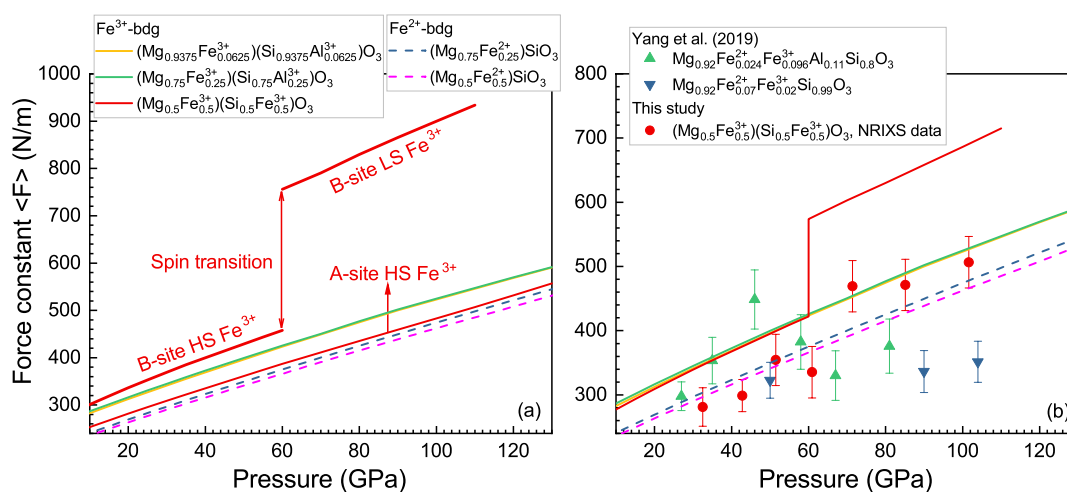
292 Here $g(E)$ is PDOS, M is the mass of a ^{54}Fe or ^{56}Fe nucleus, k is Boltzmann's constant
293 and T is temperature in Kelvin. We find that $\langle F \rangle$ obtained from calculated PDOS are
294 significantly larger than those calculated from experimental PDOS (Fig. 3), especially
295 at pressures > 60 GPa, although the calculated PDOS match well with experimental
296 PDOS (Fig. 2 and S1). To find out the factors that result in the $\langle F \rangle$ differences, we
297 calculated the evolution of $\langle F \rangle$ by changing the upper limit of energy (x) for the
298 integration by following Eq. (8):

$$299 \quad \langle F \rangle = \frac{M}{\hbar^2} \int_0^x E^2 g(E) dE, \quad (x \text{ increases from } 0 \text{ to } +\infty) \quad (8)$$

300 As shown in Fig. 4, the integral values of $\langle F \rangle$ from calculated PDOS agree well with
301 those from experimental PDOS until energy for the integration reaches a threshold,
302 above which the predicted $\langle F \rangle$ still increases with x but the experimental one
303 maintains a constant value (Fig. 4). This is mainly because the experimental PDOS
304 intensity becomes indistinguishably close to zero due to the low signal noise ratio when
305 energy is larger than 85 meV at 32.5 GPa and 110 meV at 101.4 GPa, while the
306 predicted PDOS from DFT+ U still have small non-zero values at these high-energy
307 parts (Fig. 2). Amplified by the integral $E^2 g(E)$, the small discrepancies in PDOS lead
308 to significant differences in the final $\langle F \rangle$ by ~ 60 N/m at ~ 30 GPa and ~ 154 N/m at
309 100 GPa. Similarly, the predicted PDOS of A-site Fe^{3+} and Fe^{2+} in Bdg also agree well
310 with experimental measurements (Yang et al., 2019), but the $\langle F \rangle$ from DFT+ U are
311 larger than experimental values, especially at high pressures (Fig. S3 and S4). In
312 contrast, both of the calculated PDOS and $\langle F \rangle$ of LS Fe in Fp agree well with
313 experimental results (Fig. S5). As a consequence, we use theoretical results of Bdg in
314 this study and experimental data of HS and LS Fp from Yang et al. (2019) for further
315 modelling and discussion.

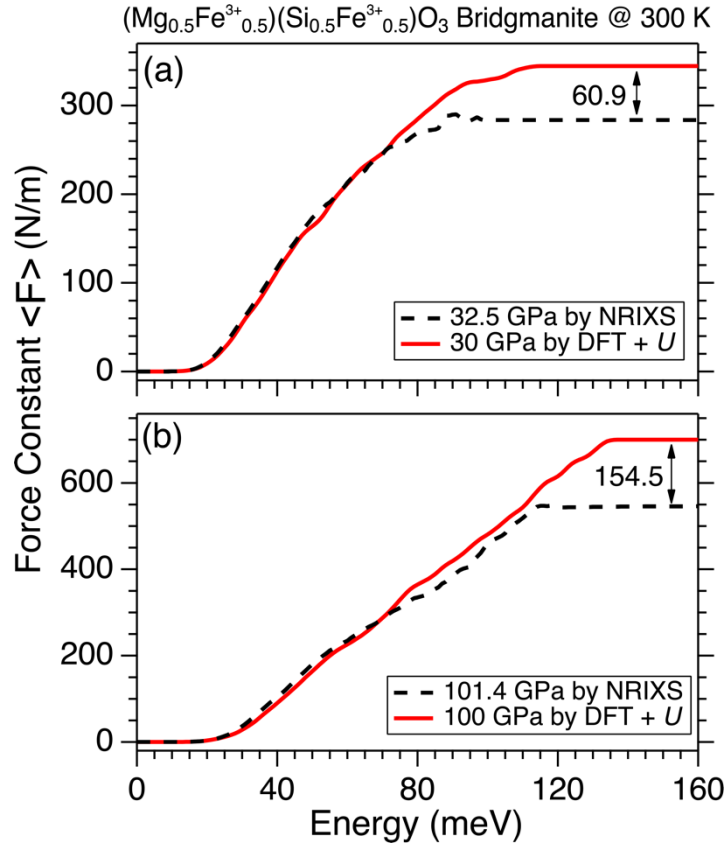
316 Blanchard et al. (2015) found that compared to NRIXS, the DFT calculations
 317 within GGA/GGA+U underestimate the $\langle F \rangle$ of iron in goethite. However, in their DFT
 318 calculations, the cell parameters of goethite were fixed to their experimental values and
 319 only atomic positions were relaxed. Because the GGA usually overestimates the volume,
 320 this incorrect strategy would put artificial stress on the structure and the true pressure
 321 from the GGA calculations should be higher than ambient pressure (Wang et al., 2017a;
 322 Wang et al., 2019b). This indicates that the iron $\langle F \rangle$ in Blanchard et al. (2015) was
 323 overestimated by their GGA/GGA+U calculations, and thus the $\langle F \rangle$ difference
 324 between NRIXS and DFT was underestimated. The discrepancy between NRIXS and
 325 GGA/GGA+U is mainly because the GGA underestimates the vibrational frequencies
 326 (Schauble, 2011), shifting the PDOS to lower values.

327 The changes of PDOS by different cation sites and spin states of Fe^{3+} result in
 328 variations in the corresponding $\langle F \rangle$ and β -factors. For instance, as the PDOS of B-site
 329 HS Fe^{3+} concentrates at higher energy range compared with the corresponding A-site
 330 HS Fe^{3+} (Fig. 2 and S1), $\langle F \rangle$ and β -factors are thus higher for HS Fe^{3+} in the B-site
 331 than that in the A-site (Fig. 3 and Fig. 5). Notably, across the spin transition of the B-
 332 site Fe^{3+} in $(\text{Mg}_{0.5}\text{Fe}^{3+}_{0.5})(\text{Si}_{0.5}\text{Fe}^{3+}_{0.5})\text{O}_3$ Bdg at ~ 60 GPa, the $\langle F \rangle$ and β -factors of B-
 333 site Fe^{3+} increases by $\sim 65\%$.



334
 335 **Figure 3.** Force constant $\langle F \rangle$ of iron in Bdg from DFT+U calculations. (a) $\langle F \rangle$ of A-site Fe^{2+} ,
 336 A-site Fe^{3+} , and B-site Fe^{3+} in Bdg. Compared with the $\langle F \rangle$ of A-site Fe^{2+} , those of both A-
 337 site and B-site Fe^{3+} in Bdg are higher at the same pressure. Across the spin transition of the B-
 338 site Fe^{3+} in $(\text{Mg}_{0.5}\text{Fe}^{3+}_{0.5})(\text{Si}_{0.5}\text{Fe}^{3+}_{0.5})\text{O}_3$ Bdg at ~ 60 GPa, the $\langle F \rangle$ of B-site Fe^{3+} increases by

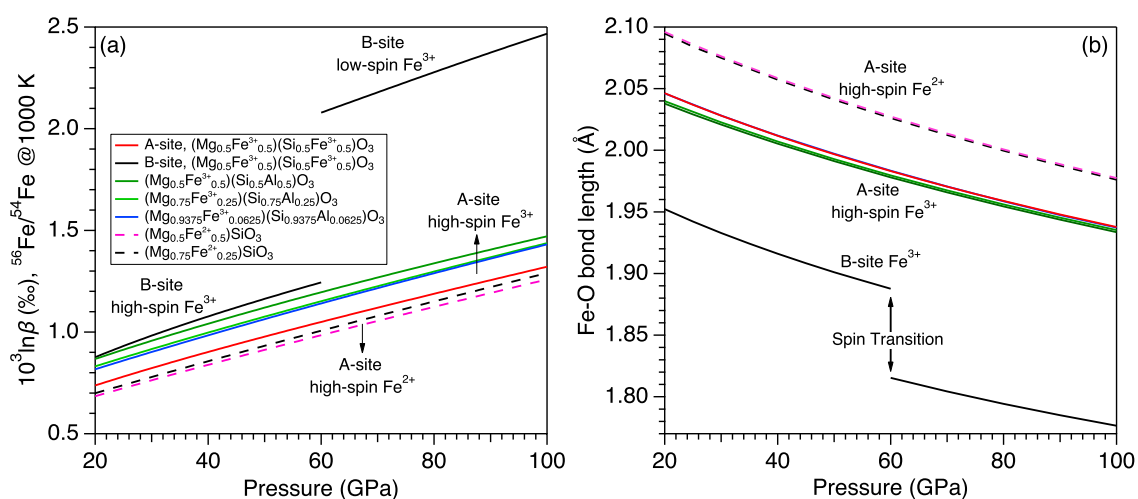
339 ~65%. **(b)** comparisons of in $\langle F \rangle$ Bdg between theoretical and experimental results (Yang et
 340 al., 2019). Although PDOS of Fe in Bdg from DFT+ U agree well with experimental
 341 measurements (Fig. 2, Fig. S1, and Fig. S3-S4), the predicted $\langle F \rangle$ are significantly larger than
 342 those from experimental PDOS, especially at high pressures.



343
 344 **Figure 4.** Evolution of $\langle F \rangle$ of Fe^{3+} in $(\text{Mg}_{0.5}\text{Fe}^{3+}_{0.5})(\text{Si}_{0.5}\text{Fe}^{3+}_{0.5})\text{O}_3$ Bdg with the upper limit of
 345 energy (x) for the integration $\langle F \rangle = \frac{M}{\hbar^2} \int_0^x E^2 g(E) dE$. The integral values of $\langle F \rangle$ from
 346 DFT+ U calculations agree well with experimental results when x reaches a threshold, above
 347 which the predicted $\langle F \rangle$ still increases with x but the experimental one maintains a constant
 348 value.

349
 350 On the other hand, the β -factors can be also calculated from Eq. (1) within the
 351 quasi-harmonic approximation (Urey equation). Following Bigeleisen and Mayer
 352 (1947) and Kowalski et al. (2013), when the β -factor is expressed by the Taylor
 353 expansions and the higher order terms are not taken into account, the Urey equation can
 354 be then approximated by Eq. (7). The validity criteria restricts the usage of Eq. (6) to
 355 frequencies $\nu [\text{cm}^{-1}] \leq 1.39T [\text{K}]$ (Bigeleisen and Mayer, 1947; Kowalski et al.,

356 2013). Here we calculated the β -factors of Bdg with different chemical compositions
 357 from their full phonon vibrational spectra using Eq. (1). Our calculated results show
 358 that the $10^3 \ln \beta$ of Bdg decreases in the order of LS- $(\text{Mg}_{0.5}\text{Fe}^{3+}_{0.5})(\text{Si}_{0.5}\text{Fe}^{3+}_{0.5})\text{O}_3 >$ HS-
 359 $(\text{Mg}_{0.5}\text{Fe}^{3+}_{0.5})(\text{Si}_{0.5}\text{Fe}^{3+}_{0.5})\text{O}_3 >$ $(\text{Mg}_{0.9375}\text{Fe}^{3+}_{0.0625})(\text{Si}_{0.9375}\text{Al}^{3+}_{0.0625})\text{O}_3 \approx$
 360 $(\text{Mg}_{0.75}\text{Fe}^{3+}_{0.25})(\text{Si}_{0.75}\text{Al}_{0.25})\text{O}_3 >$ $(\text{Mg}_{0.75}\text{Fe}^{2+}_{0.25})\text{SiO}_3 \approx (\text{Mg}_{0.5}\text{Fe}^{2+}_{0.5})\text{SiO}_3$ within
 361 calculated pressure range. At 60 GPa and 1000 K, it varies from 1.58‰ for LS-
 362 $(\text{Mg}_{0.5}\text{Fe}^{3+}_{0.5})(\text{Si}_{0.5}\text{Fe}^{3+}_{0.5})\text{O}_3$ to 0.98‰ for $(\text{Mg}_{0.5}\text{Fe}^{2+}_{0.5})\text{SiO}_3$ Bdg (Fig. 5a). Rustad and
 363 Yin (2009) also calculated the β factor of Fe^{2+} -bearing Bdg using molecular clusters
 364 and the $10^3 \ln \beta$ of $^{56}\text{Fe}/^{54}\text{Fe}$ is ~ 1.44 ‰ at 120 GPa and 1000 K, similar to our predictions
 365 (1.42 ‰). However, it should be noted that the modelling of crystals using molecular
 366 clusters breaks the intrinsic periodic boundary of crystals.
 367



368
 369 **Figure 5.** Comparisons between the $^{56}\text{Fe}/^{54}\text{Fe}$ β -factors and the Fe-O bond length of bdg at 30-
 370 100 GPa and 1000 K for different compositions in DFT+ U calculations. (a) Compared with the
 371 β -factors of Fe^{2+} in the A-site of Bdg, those of both A-site and B-site Fe^{3+} in Bdg are higher at
 372 the same P - T condition. Across the spin transition of the B-site Fe^{3+} in
 373 $(\text{Mg}_{0.5}\text{Fe}^{3+}_{0.5})(\text{Si}_{0.5}\text{Fe}^{3+}_{0.5})\text{O}_3$ Bdg at ~ 60 GPa, the $^{56}\text{Fe}/^{54}\text{Fe}$ β -factor of B-site Fe^{3+} at 1000 K
 374 increases by 0.835‰. (b) The average Fe-O bond lengths in Bdg with different compositions
 375 at static conditions. Across the spin transition of B-site Fe^{3+} in $(\text{Mg}_{0.5}\text{Fe}^{3+}_{0.5})(\text{Si}_{0.5}\text{Fe}^{3+}_{0.5})\text{O}_3$ Bdg
 376 at ~ 60 GPa, the lengths of A-site and B-site Fe^{3+} decrease by 0.014 Å and 0.072 Å,
 377 respectively. In contrast, the concentration effect on both A-site Fe^{2+} -O and A-site Fe^{3+} -O bond
 378 lengths in Bdg is negligible.

379

380 4. Discussion

381 4.1 Effects of site occupancy, spin transition, chemical composition, and valence 382 state on β -factors of Bdg

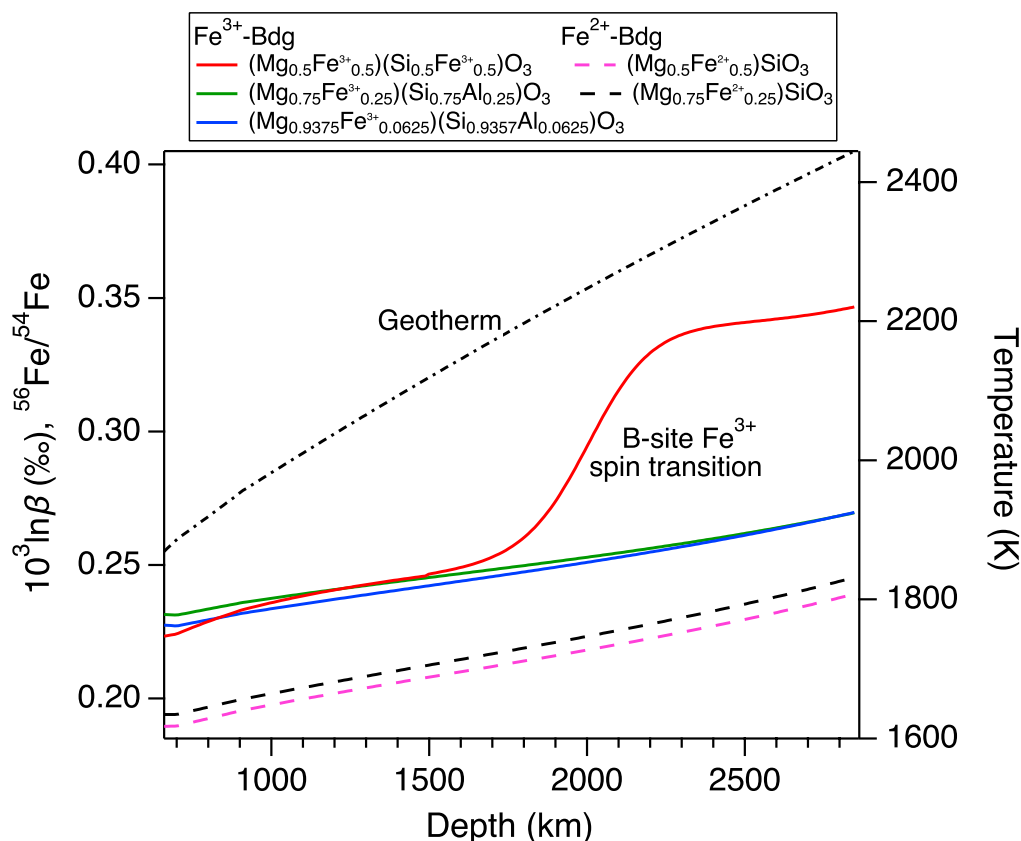
383 The pressure dependences of β -factors of Bdg are controlled by multiple factors
384 as shown in Fig. 2a. Here we show the β -factors anchored at 1000 K as a representative
385 temperature to address these effects since the factors are almost linearly proportional to
386 $1/T^2$ at different pressures (Fig. S6). In $(\text{Mg}_{0.5}\text{Fe}^{3+}_{0.5})(\text{Si}_{0.5}\text{Fe}^{3+}_{0.5})\text{O}_3$ Bdg, compared to
387 the A-site HS Fe^{3+} , B-site HS Fe^{3+} has a higher β -factor and the difference between two
388 sites is $\sim 0.17\%$ at 40 GPa and 1000 K (Fig. 5a). This is also consistent with the much
389 shorter bond lengths, and correspondingly higher bond strength, of Fe^{3+} -O in the 6-
390 coordinated B-site relative to the 8-coordinated A-site (Fig. 5b). B-site Fe^{3+} in Bdg is
391 expected to undergo a HS to LS transition at middle-mantle depths (Catalli et al., 2010;
392 Hsu et al., 2011; Mao et al., 2015; Shukla and Wentzcovitch, 2016; Fu et al., 2018b;
393 Liu et al., 2018). The spin transition of the B-site Fe^{3+} in $(\text{Mg}_{0.5}\text{Fe}^{3+}_{0.5})(\text{Si}_{0.5}\text{Fe}^{3+}_{0.5})\text{O}_3$
394 Bdg occurs at ~ 50 GPa (Liu et al., 2018), which leads to shortening of the average B-
395 site Fe^{3+} -O bonds by 0.072 Å, equal to 3.8% relative change (Fig. 5b). Such a change
396 in the average Fe-O bond induces an increase of 0.83% in the β -factor of B-site Fe^{3+} at
397 1000 K and 0.21% at 2000 K (Fig. S6). However, the spin transition of the B-site Fe^{3+}
398 does not significantly change the A-site Fe^{3+} -O bonds and the β -factor of A-site Fe^{3+} .
399 Thus, the contrast between the β -factors of B-site and A-site Fe^{3+} is also strongly
400 enhanced by the Fe spin transition in the B-site from 0.19% to 1.01% at 1000 K and
401 60 GPa (Fig. 5a).

402 The presence of Al in Bdg will weaken the effect of B-site Fe^{3+} spin transition on
403 its β -factor by preventing Fe^{3+} from occupying the B-site. Depending on the bulk
404 Al/ Fe^{3+} molar ratio, Al^{3+} can either occupy the B-site only with Fe^{3+} filling in the A-
405 site or it occupies both the B-site and the available A-site left by A-site Fe^{3+} (Lin et al.,
406 2013; Liu et al., 2015). For Al/ Fe^{3+} molar ratio equal to 1, all Fe^{3+} would occupy the A-
407 site and all Al stays in the B-site. Here we calculated the β -factors of three Fe^{3+} - and
408 Al-bearing Bdg with different FeAlO_3 concentration at 1000 K to illustrate the
409 compositional dependence of both Fe^{3+} -O bond length and the β -factor of $^{56}\text{Fe}/^{54}\text{Fe}$ (Fig.

410 5a). Our results show that the incorporation of 6.25-50 mol% FeAlO₃ into Bdg only
 411 changes the A-site Fe³⁺-O bond length by 0-0.007 Å under lower-mantle pressures (Fig.
 412 5b). As the Fe-O bond length controls the magnitude of the corresponding β-factor (Fig.
 413 S7), the effect of FeAlO₃ concentration on the β-factors of the A-site Fe³⁺ is
 414 insignificant. For example, the largest difference in the β-factor of Al³⁺- and Fe³⁺-
 415 bearing Bdg (Mg_{0.9375}Fe³⁺_{0.0625})(Si_{0.9375}Al³⁺_{0.0625})O₃, (Mg_{0.75}Fe³⁺_{0.25})(Si_{0.75}Al_{0.25})O₃,
 416 and (Mg_{0.5}Fe³⁺_{0.5})(Si_{0.5}Al³⁺_{0.5})O₃ is smaller than 0.06‰ at 1000 K and all pressures (Fig.
 417 5a). In contrast, the β-factor of A-site Fe³⁺ in (Mg_{0.5}Fe³⁺_{0.5})(Si_{0.5}Al³⁺_{0.5})O₃ Bdg is ~ 0.14‰
 418 larger than that of A-site Fe³⁺ in (Mg_{0.5}Fe³⁺_{0.5})(Si_{0.5}Fe³⁺_{0.5})O₃ Bdg, consistent with
 419 relatively shorter Fe³⁺-O bonds in the A site of (Mg_{0.5}Fe³⁺_{0.5})(Si_{0.5}Al³⁺_{0.5})O₃ Bdg (Fig.
 420 5b). This reveals that the speciation of B-site ion (Fe³⁺ or Al³⁺) also has a mild effect
 421 on the A-site Fe³⁺-O bond strength and its β-factor. However, such an effect of Al on
 422 A-site Fe³⁺ β-factor is much weaker than the influence of spin transition and can be
 423 further diminished by mantle high temperatures, which results in only 0-0.01‰
 424 difference in β-factor along the normal lower-mantle geotherm (Fig. 6). As long as
 425 some Fe³⁺ occupies the Bdg B-site, the change in β-factor due to the spin transition is
 426 independent of the identity of other ions on A- and B-site. Therefore, although Al³⁺
 427 incorporation itself does not change the Bdg structure enough to impact isotopic
 428 fractionation, it prevents Fe³⁺ from occupying the B-site and thus reduces the significant
 429 impact of B-site Fe³⁺ spin transition on the β-factor of Bdg.

430 In addition to Fe³⁺, the A site in Bdg is also large enough to accommodate Fe²⁺,
 431 which maintains a HS state in Bdg throughout the lower mantle. The Fe²⁺-bearing Bdg
 432 compositions in our DFT+*U* calculations, (Mg_{0.5}Fe²⁺_{0.5})SiO₃ and (Mg_{0.75}Fe²⁺_{0.25})SiO₃,
 433 have the smallest β-factors that are also insensitive to the Fe²⁺ content (Fig. 5a). This
 434 difference in β-factor between A-site Fe³⁺ and Fe²⁺ ranges from 0.04‰ to 0.15‰ at
 435 1000 K (Fig. 5a) but will be diminished along an expected geotherm of the lower mantle
 436 (Fig. 6). In particular, the β-factor increases with pressure along the adiabat, because
 437 the increase due to compression outweighs the decrease from the 1/T² dependence. The
 438 enrichment of light Fe isotopes in Fe²⁺-bearing Bdg relative to other Fe³⁺-bearing
 439 species is mainly caused by the longer Fe²⁺-O bond lengths than those Fe³⁺-O bonds
 440 (Fig. 5b and S7). Moreover, the valence state also partially contributes to the smaller β-

441 factors of Fe^{2+} -bearing Bdg as revealed by the longer Fe-O bond length of HS A-site
 442 Fe^{2+} than that of HS A-site Fe^{3+} (Fig. S7). In summary, the pressure- and temperature
 443 dependent β -factor of $^{56}\text{Fe}/^{54}\text{Fe}$ for Bdg is controlled by the $\text{Fe}^{3+}/\text{Fe}^{2+}$, Al/Fe^{3+} , and spin
 444 transition if there is some Fe^{3+} accommodated in B site.
 445



446
 447 **Figure 6.** $^{56}\text{Fe}/^{54}\text{Fe}$ β -factors of various Bdg compositions computed by DFT+ U along an
 448 adiabat representative of the average lower mantle. As the B-site Fe^{3+} undergoes high-spin to
 449 low-spin transition, the $^{56}\text{Fe}/^{54}\text{Fe}$ β -factor of $(\text{Mg}_{0.5}\text{Fe}^{3+}_{0.5})(\text{Si}_{0.5}\text{Fe}^{3+}_{0.5})\text{O}_3$ Bdg increases by
 450 $\sim 0.09\%$ across the spin transition of the B-site Fe^{3+} . The expected geotherm (dot dash line) was
 451 taken from Brown and McQueen (1986).

452

453 4.2 Fe isotopic fractionation in the deep mantle

454 4.2.1 Inter-mineral iron isotope fractionation

455 The $^{56}\text{Fe}/^{54}\text{Fe}$ β -factor of Bdg and Fp as a function of depth in likely bulk mantle
 456 compositions can be used to estimate fractionation of Fe isotopes in the deep Earth. The
 457 depth-dependence of Fe isotopic fractionation between Bdg and Fp in the lower mantle

458 is modelled based on the following equations:

$$459 \quad \Delta^{56}\text{Fe}_{\text{Bdg-Fp}} = \delta^{56}\text{Fe}_{\text{Bdg}} - \delta^{56}\text{Fe}_{\text{Fp}} \quad (9)$$

$$460 \quad \delta^{56}\text{Fe}_{\text{LM}} = n_{\text{Bdg}} \times \delta^{56}\text{Fe}_{\text{Bdg}} + n_{\text{Fp}} \times \delta^{56}\text{Fe}_{\text{Fp}} \quad (10)$$

461 where $\delta^{56}\text{Fe}_{\text{Bdg}}$, $\delta^{56}\text{Fe}_{\text{Fp}}$, and $\delta^{56}\text{Fe}_{\text{LM}}$ are the Fe isotopic compositions of Bdg, Fp, and
462 the bulk lower mantle, respectively. $\delta^{56}\text{Fe}_{\text{LM}}$ is set to 0 as the representative chondritic
463 value (Craddock and Dauphas, 2011). n_{Bdg} and n_{Fp} are the Fe fractions in Bdg and Fp
464 (Table S1), respectively, based on a pyrolitic lower mantle composition (Irifune et al.,
465 2010). The pressure effect, including the pressure-induced spin transition, is taken into
466 account on the evaluation of β -factors of Bdg and Fp.

467 Previous studies (Wang et al., 2015; Zhang et al., 2016; Wu, 2016) suggested that
468 the lower mantle may be represented by a pyrolitic composition with ~ 8 wt% FeO and
469 a Al/Fe ratio ~ 0.8 (McDonough and Sun, 1995). The lower-mantle $\text{Fe}^{3+}/\Sigma\text{Fe}$ ratio range
470 was thought to be higher than 0.5 (Frost and McCammon, 2008), and the $\text{Fe}^{3+}/\Sigma\text{Fe}$ ratio
471 of Bdg could be 0.5-1 for most part of the lower mantle (Wang et al., 2015). Because
472 the site occupancy of Fe^{3+} is controlled by $\text{Al}^{3+}/\text{Fe}^{3+}$ ratios (Frost et al., 2004; Lin et al.,
473 2013; Liu et al., 2015; Liu et al., 2018), we consider three different endmembers for
474 Bdg compositions: (1) Fe^{3+} - and Al^{3+} -free, Fe^{2+} -bearing; (2) Fe^{3+} - and Al^{3+} -bearing (3)
475 Fe^{3+} -bearing but Al^{3+} -free (Fig. 7). These three endmembers demonstrate the range of
476 possible compositional effects on Fe isotopic compositions of Bdg and Fp in the lower
477 mantle:

- 478 1) For a simplified Fe^{3+} - and Al^{3+} -free, Fe^{2+} -bearing system, the major factor that
479 impacts Fe-O bonds and Fe isotopic fractionation is the spin transition of Fe^{2+}
480 in Fp at mid-lower-mantle depths. In this system, there is no significant iron
481 fractionation between Bdg and Fp ($\Delta^{56}\text{Fe}_{\text{Bdg-Fp}} = 0-0.02\text{‰}$) below 60 GPa. The
482 spin transition occurs only in Fp at $\sim 60-120$ GPa, and increases the β -factor of
483 Fp. This effect significantly decreases $\Delta^{56}\text{Fe}_{\text{Bdg-Fp}}$ from 0‰ at ~ 60 GPa to -0.17‰
484 at ~ 120 GPa (Fig. 7a). As a result, Fp would be enriched in ^{56}Fe with $\delta^{56}\text{Fe}_{\text{Fp}}$
485 up to $0-0.08\text{‰}$ below mid-lower mantle and $\delta^{56}\text{Fe}_{\text{Bdg}}$ would be as low as -0.07‰
486 (Fig. 7b).
- 487 2) For a more realistic Fe^{3+} - and Al^{3+} -bearing system with the Fe^{3+}/Al ratio of < 1 ,
488 our computational results suggest that the presence of Fe^{3+} in the Bdg A-site

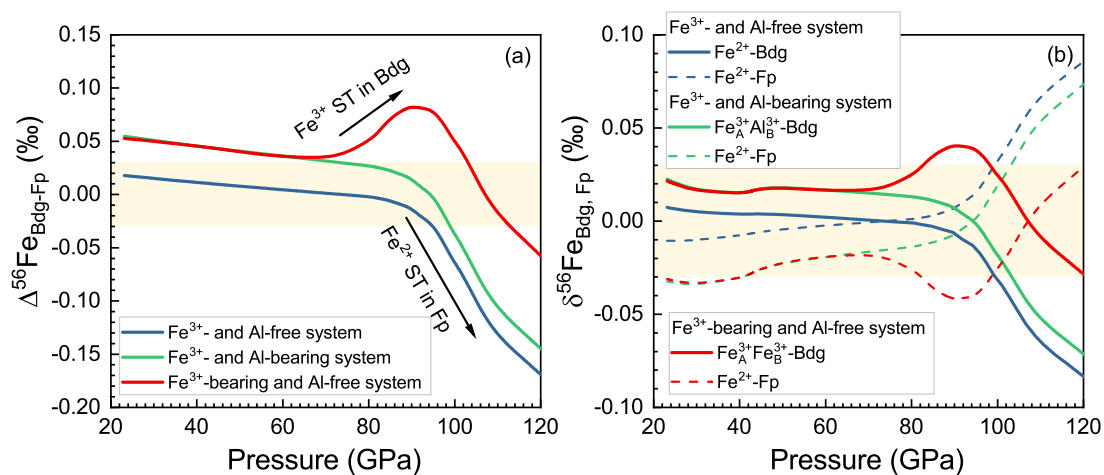
489 increases the β -factor of Bdg by 0.03-0.04‰ along an expected geotherm (Fig.
490 6). No significant difference across the spin transition of B-site Fe^{3+} in Bdg is
491 expected in this composition relative to the Fe^{3+} - and Al^{3+} -free, but Fe^{2+} -bearing
492 system. Therefore, $\Delta^{56}\text{Fe}_{\text{Bdg-Fp}}$ of the Fe^{3+} - and Al^{3+} -bearing system is ~ 0.03 -
493 0.04% higher than that of the simplified Fe^{3+} - and Al^{3+} -free, Fe^{2+} -bearing
494 system (Fig. 7a). In this case, $\Delta^{56}\text{Fe}_{\text{Bdg-Fp}}$ decreases from $+0.05\%$ in the upper
495 part of the lower mantle to -0.15% in the deeper part (Fig. 7b). This results in
496 $\delta^{56}\text{Fe}_{\text{Bdg}}$ of $+0.02\%$ in the uppermost lower mantle but the number decreases to
497 $\sim -0.07\%$ in the lowermost lower mantle (Fig. 7b).

498 3) In a Fe^{3+} - bearing but Al^{3+} -free system, the spin transitions of both Fe^{2+} in Fp
499 and B-site Fe^{3+} in Bdg are expected to occur at the middle mantle depths and
500 extend to the deeper part (Fig. 7a). Consequently, $\Delta^{56}\text{Fe}_{\text{Bdg-Fp}}$ in Fe^{3+} - bearing
501 and Al^{3+} -free system is significantly higher than the other two systems beneath
502 the middle mantle depths (Fig. 7a). The spin transition in B-site Fe^{3+} of Bdg
503 results in $\delta^{56}\text{Fe}_{\text{Bdg}}$ as high as $+0.04\%$ in the middle mantle depth, which
504 decreases to -0.03% in the lowermost lower mantle (Fig. 4b).

505 In a pyrolitic lower mantle, Fe^{3+} is generally not expected to occupy the B-site of
506 Bdg as the Al/Fe^{3+} ratios of synthesized Bdg samples from pyrolitic starting materials
507 are consistently higher than 1 (summarized in Shim et al., 2017). Harzburgite has a
508 similar iron content but less Al_2O_3 content ($\sim 0.6\%$) compared to pyrolite (Irfune and
509 Ringwood, 1987) and its $\text{Fe}^{3+}/\Sigma\text{Fe}$ ratio is usually $< 5\%$ (Canil and O’Neill, 1996;
510 Woodland et al., 2006). As such, the Fe^{3+}/Al ratio in harzburgite is typically < 0.5 and
511 no Fe^{3+} would occupy the B-site of Bdg when Bdg crystallizes from a harzburgitic
512 composition. Therefore, the $\Delta^{56}\text{Fe}_{\text{Bdg-Fp}}$ in a pyrolitic or harzburgitic composition is
513 similar to the results in scenarios (1) and (2). On the other hand, Fe^{3+} -rich materials
514 (such as banded iron formation and goethite) could be carried to the lower mantle by
515 subducted slabs, resulting in local chemical heterogeneous regions enriched in Fe^{3+} .
516 Under such a scenario, Bdg may have much lower Al content and higher Fe^{3+} content,
517 and therefore more Fe^{3+} could occupy both the A-site and B-site by the coupled
518 substitution mechanism (Frost et al., 2004; Liu et al., 2015; Shim et al., 2017; Liu et al.,
519 2018). Compared with Fe^{3+} - and Al^{3+} -bearing Bdg forming in a pyrolitic composition,

520 the spin transition of the B-site Fe^{3+} in Bdg would increase $\Delta^{56}\text{Fe}_{\text{Bdg-Fp}}$ by as much as
 521 0.08‰ (Fig. 7b), which slightly exceeds the highest precision measurements of $\delta^{56}\text{Fe}$
 522 ($\sim 0.03\%$, Sossi et al., 2015). Overall, Fe isotopic fractionation between Bdg and Fp is
 523 insignificant in most parts of the lower mantle, except the lowermost parts (Fig. 7). In
 524 the upper and middle part of the lower mantle, the stronger Fe-O bond strength in Fe^{3+} -
 525 enriched Bdg would only enrich Bdg in ^{56}Fe with $\delta^{56}\text{Fe}_{\text{Bdg}}$ as high as $+0.02\%$, with
 526 correspondingly indistinguishable $\Delta^{56}\text{Fe}_{\text{Bdg-Fp}}$ in these depths based on the highest
 527 precision of MC-ICP-MS measurements ($\sim 0.03\%$, Sossi et al., 2015). In the lowermost
 528 lower mantle, the spin transition of Fe^{2+} in Fp would lead to the enrichment of heavy
 529 Fe in Fp with $\Delta^{56}\text{Fe}_{\text{Bdg-Fp}}$ as low as -0.15% in a pyrolitic composition. For the Fe^{3+} -rich
 530 but Al-poor system, the spin transition of B-site Fe^{3+} in Al-poor Bdg would diminish
 531 $\Delta^{56}\text{Fe}_{\text{Bdg-Fp}}$, making the Fe isotopic compositions of the coexisting oxidized Bdg and Fp
 532 indistinguishable (Fig. 7b). Therefore, the magnitude of $\Delta^{56}\text{Fe}_{\text{Bdg-Fp}}$ in a pyrolitic
 533 composition would probably exceed the technical resolution for Fe isotope
 534 measurements in the lowermost lower mantle, whereas no significant $\Delta^{56}\text{Fe}_{\text{Bdg-Fp}}$ would
 535 be found in the Fe^{3+} -rich but Al-poor system.

536



537

538 **Figure 7.** Equilibrium $^{56}\text{Fe}/^{54}\text{Fe}$ isotopic fractionation between coexisting Bdg and Fp (a) and
 539 the corresponding Fe isotopic compositions of these two phases (b) along an expected geotherm
 540 (Brown and McQueen, 1986). Solid and dash lines in (b) represent Fe isotopic compositions of
 541 Bdg and Fp, respectively. Three compositional assemblages are considered: Fe^{3+} -bearing but
 542 Al-free system (red curves); Fe^{3+} - but Al-bearing system (green curves) and Fe^{3+} - and Al-free
 543 system (blue curves). The light yellow areas represent the best resolution of MC-ICP-MS

544 measurements (~ 0.03%, Sossi et al., 2015). The spin transition (ST) of Fe²⁺ in Fp would occur
545 at the middle depth of the lower mantle, where only the B-site Fe³⁺ in Bdg would undergo a HS
546 to LS transition at ~60 GPa.

547

548 **4.2.2 Iron isotope fractionation during magma ocean crystallization**

549 In addition to the possible Fe isotope fractionation between solid phases, how Fe
550 isotopes would be fractionated between silicate melts and minerals during magma
551 ocean crystallization (Boukaré et al., 2015) is also important for understanding the
552 variability in iron isotopic composition in deep mantle (Yang et al., 2019). Based on the
553 $\langle F \rangle$ of solid phases and basaltic glass, Yang et al. (2019) investigated the evolution of
554 Fe isotopic fractionation during terrestrial magma ocean crystallization and found no
555 significant Fe fractionation between minerals and silicate melts. Here, following the
556 model proposed in Yang et al. (2019), we also reevaluated the Fe isotope fractionation
557 between Bdg+Fp and silicate melts during magma ocean crystallization using the $\langle F \rangle$
558 of Bdg from DFT+*U* calculations in this study. The $\langle F \rangle$ of solid phase was calculated
559 from the $\langle F \rangle$ of Fp and Bdg using $\langle F \rangle_{\text{sum}} = n_{\text{Fp}} * \langle F \rangle_{\text{Fp}} + n_{\text{Bdg}} * \langle F \rangle_{\text{Bdg}}$, where n_{Fp} and n_{Bdg}
560 are the fractions of iron in Fp and Bdg in the solid phase, respectively, and $n_{\text{Fp}} + n_{\text{Bdg}} = 1$.
561 The $\langle F \rangle$ of basaltic glass extrapolated to 130 GPa was used as an analogue to basaltic
562 melts (Liu et al., 2017). The chemical compositions of solid aggregates and the residual
563 melt were calculated after each 1 wt% increment of crystallization and can be found in
564 Yang et al. (2019). Fractional crystallization and a mass-balance relationship were used
565 in the model. For the *i*th separation of solids, the isotopic composition of solids
566 equilibrated with the residual melt can be calculated by $\delta^{56}\text{Fe}_{\text{solids-}i+1} = \delta^{56}\text{Fe}_{\text{melts-}i}$
567 $+ \Delta^{56}\text{Fe}_{\text{solids-melts}}$. Based on the isotopic mass balance, we have:

$$568 \delta^{56}\text{Fe}_{\text{melts-}i+1} = [\delta^{56}\text{Fe}_{\text{melts-}i} - (\delta^{56}\text{Fe}_{\text{melts-}i} + \Delta^{56}\text{Fe}_{\text{solids-melts}}) * n_{\text{solid}}] / (1 - n_{\text{solids}}) \quad (11)$$

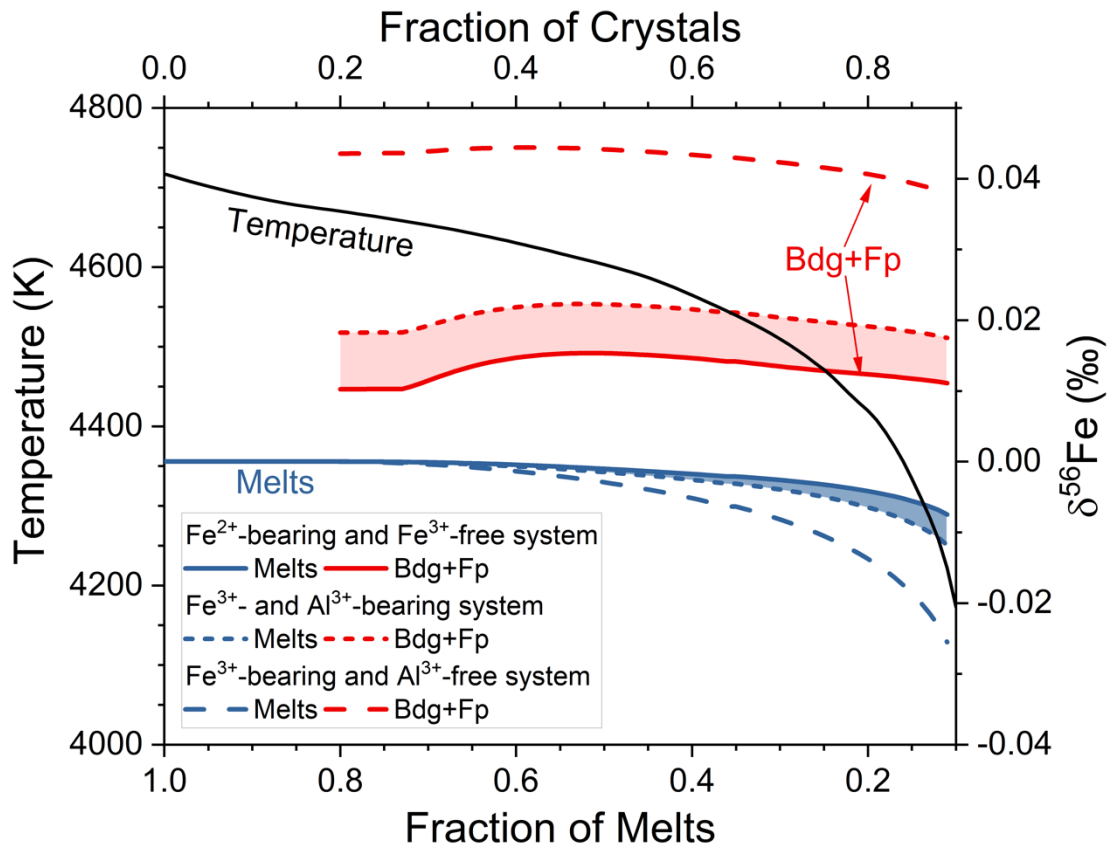
$$569 \delta^{56}\text{Fe}_{\text{solids-}i+1} = -\delta^{56}\text{Fe}_{\text{melts-}i+1} * n_{\text{melts}} / (1 - n_{\text{melts}}) \quad (12)$$

570 where n_{solids} is the fraction of iron taken up by solids at each step and n_{melts} is the fraction
571 of total iron in the remaining melt. We note that the chemical composition of residual
572 melt would be dominated by FeO (Fe/(Fe+Mg) > 60%) when the fraction of melt is
573 lower than 10% with temperature decreasing to 4200 K (Figure 7 in Boukaré et al.,
574 2015). At this stage, the $\langle F \rangle$ of basaltic glass may not be used as an analogue to silicate

575 melts due to the large difference in chemical compositions, and we stopped the
576 simulations.

577 Our results show that silicate melts are isotopically lighter than Bdg+Fp but the
578 $\Delta^{56}\text{Fe}_{\text{solids-melts}}$ are smaller than +0.03‰ for Fe^{2+} -bearing and Fe^{3+} -free systems and
579 Fe^{3+} - and Al^{3+} -bearing system. As Fe^{3+} is generally not expected to occupy the Bdg B-
580 site in a pyrolytic lower mantle with the Al/Fe^{3+} ratios of higher than 1, it can be
581 concluded that no significant Fe isotope fractionation between Bdg+Fp and silicate melt
582 has been produced during the crystallization process. For the Fe^{3+} -bearing but Al-poor
583 system, $\Delta^{56}\text{Fe}_{\text{solids-melts}}$ could be up +0.06‰, if we also used the $\langle F \rangle$ of basaltic melts
584 as an analogue to Fe^{3+} -rich melts. However, Fe^{3+} -rich melts should be expected to be
585 enriched in heavy Fe isotopes relative to the Fe^{2+} -rich one (Dauphas et al., 2014),
586 because the $\langle F \rangle$ of Fe^{3+} -bearing silicate glass is ~ 150 N/m larger than that of Fe^{2+} -
587 bearing silicate glass (Dauphas et al., 2014). As a result, the $\langle F \rangle$ of Fe^{3+} -rich melts
588 were underestimated in this case and the $\Delta^{56}\text{Fe}_{\text{solids-melts}}$ (up +0.06‰) could have been
589 overestimated by 0.025‰, if the $\langle F \rangle$ difference between Fe^{3+} -rich and Fe^{2+} -rich melts
590 at 130 GPa is modeled by the value for silicate glasses at ambient pressure (Dauphas et
591 al., 2014). Although the $\langle F \rangle$ of Fe^{3+} -rich melts at 130 GPa are still unknown, the
592 crystallization process of Fe^{3+} -rich melts in some local regions also cannot produce
593 resolvable Fe isotope fractionation between solids and melts. Therefore, we suggest
594 that crystallization of the magma ocean is unlikely to have resulted in significant iron
595 isotopic fractionation in deep mantle.

596



597

598 **Figure 8.** Equilibrium Fe isotope fractionation between solids and melts during magma ocean
 599 crystallization at 130 GPa. The modelling details were described in details in Yang et al. (2019).
 600 Similarly, the initial $\delta^{56}\text{Fe}$ of magma ocean is set as 0‰ and the solid crystallization sequence
 601 was obtained from Boukaré et al. (2015). Red and blue lines represent $\delta^{56}\text{Fe}$ of solids (Bdg+Fp)
 602 and melts, respectively. Solid, short dash, and dash lines refer to Fe^{2+} -bearing and Fe^{3+} -free,
 603 Fe^{3+} - and Al^{3+} -bearing, and Fe^{3+} -bearing and Al^{3+} -free systems, respectively. The $\langle F \rangle$ of solids
 604 and melts at 130 GPa are used for modelling. Data sources: Bdg, DFT+ U calculations in this
 605 study; Fp, extrapolated to 130 GPa, Yang et al. (2019); melts, imitated by basaltic glass,
 606 extrapolated to 130 GPa (Liu et al., 2017). The case for a pyrolitic composition, in which both
 607 Fe^{2+} and Fe^{3+} could be present but Fe^{3+} is not expected to occupy the Bdg B-site, can be
 608 represented by shade areas enclosed by solid and short dash lines.

609

610 4.3 Fe isotope fractionation between core and mantle

611 Mid-ocean ridge basalts (MORB) in the Earth were found to be enriched in heavy
 612 Fe isotopes ($^{56}\text{Fe}/^{54}\text{Fe}$) by $\sim +0.1\%$ relative to the chondrites (Teng et al., 2013), while
 613 basalts from Mars and Vesta have Fe isotope compositions similar to the chondrites

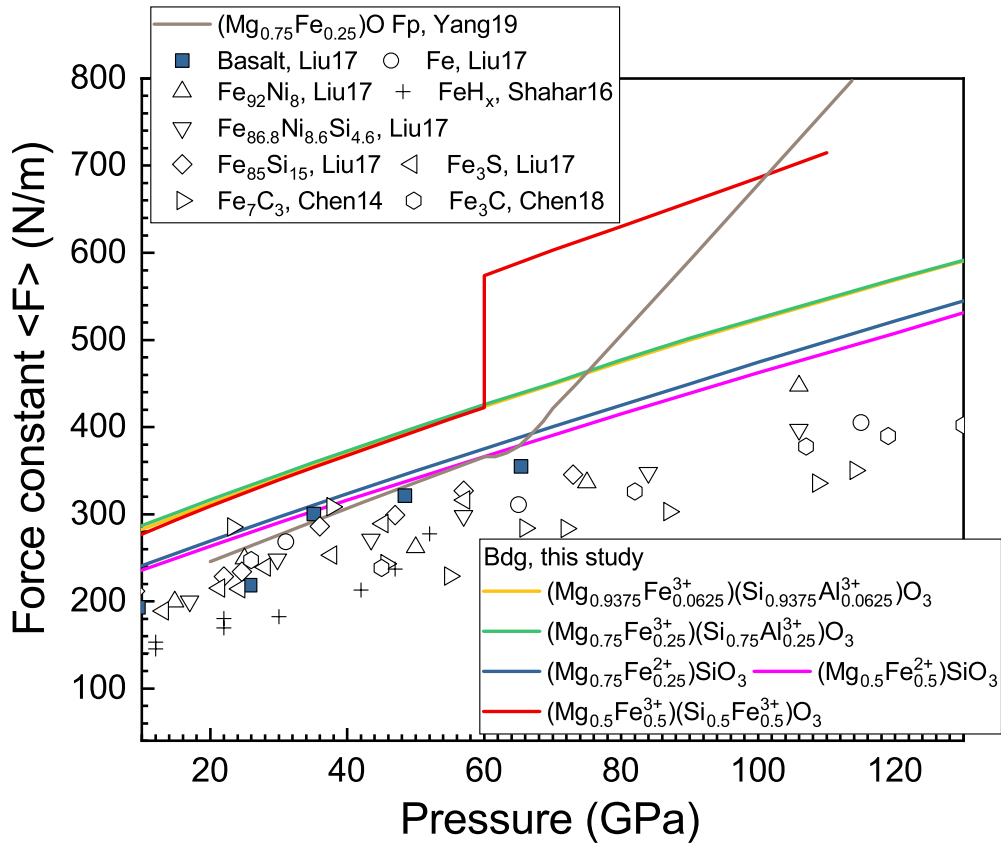
614 (Sossi et al., 2016; Elardo and Shahar, 2017). The elevated $^{56}\text{Fe}/^{54}\text{Fe}$ ratio in MORB
615 was thought to be caused by mantle partial melting (Teng et al., 2008; Dauphas et al.,
616 2014), but this process can only induce an iron isotopic shift of +0.023‰ (Dauphas et
617 al., 2014). Some other interpretations, including loss of light Fe isotopes during
618 vaporization and condensation (Poitrasson et al., 2004; Poitrasson, 2007), core
619 formation (Polyakov, 2009; Elardo and Shahar, 2017), have been proposed to enrich
620 Earth's mantle in heavy Fe isotopes. Some studies suggested that the Fe isotope
621 composition of mantle peridotites is close to that of chondrites (Poitrasson, 2007;
622 Craddock et al., 2013), while it has been argued that mantle peridotites may be slightly
623 heavier ($\sim+0.05$ ‰) than chondrites (Poitrasson et al., 2013; Sossi et al., 2016). It is not
624 well-known whether the Fe isotope composition of the primitive mantle has been
625 modified by core formation.

626 In order to check the effect of core formation on the Fe isotope composition of
627 bulk silicate Earth, previous studies have widely investigated the $\langle F \rangle$ of metallic alloys
628 (Chen et al., 2014; Shahar et al., 2016; Liu et al., 2017; Chen et al., 2018) and basaltic
629 glass (Liu et al., 2017), which were used as analogues to metallic and silicate melts,
630 respectively. In addition, Fe^{2+} -bearing Bdg was also used as the analogue to silicate
631 melt (Shahar et al., 2016). Here we also assume that the $\langle F \rangle$ of silicate melts could be
632 represented by those of Bdg, as we find that Fe^{2+} -bearing and Fe^{3+} -free Bdg has similar
633 $\langle F \rangle$ to the Fe^{2+} -bearing basaltic glass at 40-60 GPa (Fig. 9). Our results show that Bdg
634 has relatively larger $\langle F \rangle$ than metallic alloys and the $\langle F \rangle$ difference between Bdg and
635 metallic alloys depends on their chemical compositions (Fig. 9). Using the high-
636 temperature approximation, we conclude that the equilibrium Fe isotope fractionation
637 between silicate and metallic melts is $\sim 0-0.04$ ‰ under core-formation conditions for
638 the Earth ($\sim 40-60$ GPa and 3500 K) (Li and Agee, 1996; Siebert et al., 2012; Fischer et
639 al., 2015). This implies that core formation can only shift the Fe isotope composition
640 of Earth's mantle by $0-0.04$ ‰, which is not sufficient to account for the enrichment of
641 heavy Fe isotopes in MORB with the consideration of partial melting.

642 In contrast, heavy Fe isotopes might be enriched in the lowermost lower mantle
643 with respect to the adjacent liquid outer core, as low-spin Fe species likely to be present
644 in phases at the base of the mantle are expected to have high β -factors and

645 corresponding force constants $\langle F \rangle$ (Fig. 9). At P - T conditions near the CMB, Fe^{2+} is
646 expected to adopt LS state in both solid and liquid FeO-MgO system (Mao et al., 2011;
647 Fu et al., 2018a; Yang et al., 2019); while Fe^{3+} in the octahedral site of both Bdg and
648 Ppv is expected to adopt LS state (Catalli et al., 2010; Yu et al., 2012; Liu et al., 2018).
649 At a representative P - T condition near the CMB (130 GPa and 3000 K), the calculated
650 $\Delta^{56}\text{Fe}_{\text{Bdg-core}}$ from the corresponding $\langle F \rangle$ with LS Fe^{3+} in the B-site of Bdg could range
651 from +0.09‰ to +0.12‰ for various outer core compositions, such as Si, S and C (Fig.
652 9), if there is a chemical exchange and equilibration of solid mantle with outer
653 core. $(\text{Fe}^{2+}, \text{Mg})\text{SiO}_3$ -Ppv was found to be enriched in heavy iron isotopes relative to
654 metallic iron with $\Delta^{56}\text{Fe}_{\text{Ppv-core}}$ of $\sim 0.1\%$ at the CMB (Polyakov, 2009), and Fe^{3+} -
655 bearing Ppv should be more enriched in heavy iron isotopes. Meanwhile, $\Delta^{56}\text{Fe}_{\text{Fe-core}}$
656 ranges from +0.17‰ to +0.20‰ for CMB regions with high concentrations of LS FeO,
657 such as some ultra-low velocity zones (Wicks et al., 2010; Fu et al., 2018a). These
658 fractionation factors suggest that Fe isotopes might be redistributed during the mantle-
659 core interaction and some local regions above the CMB could be enriched in heavy Fe
660 isotopes. However, whether such a Fe isotopic signature could be produced and
661 preserved or not also depends on the interaction pattern and the geodynamic mantle
662 convention (Leshner et al., 2020).

663



664

665 **Figure 9.** Comparison of force constants $\langle F \rangle$ of Bdg computed in this work with previous
 666 studies of Fp and Fe/Fe alloys. At a given P - T condition, Fe equilibrium isotopic fractionation
 667 factor can be obtained by following $\Delta^{56}\text{Fe}_{\text{A-B}} = 2940 (\langle F \rangle_{\text{A}} - \langle F \rangle_{\text{B}}) / T^2$. Experimental data sources:
 668 Bdg, this study; $(\text{Mg}_{0.75}\text{Fe}_{0.25})\text{O}$ Fp, Yang et al. (2019); Basaltic
 669 glass $(\text{Na}_{0.036}\text{Ca}_{0.220}\text{Mg}_{0.493}\text{Fe}_{0.115}\text{Al}_{0.307}\text{Ti}_{0.012}\text{K}_{0.002}\text{Si}_{0.834}\text{O}_3)$, Fe, $\text{Fe}_{86.8}\text{Ni}_{8.6}\text{Si}_{4.6}$, $\text{Fe}_{85}\text{Si}_{15}$, Fe_3S :
 670 Liu et al. (2017); Fe_7C_3 : Chen et al. (2014); Fe_3C : Chen et al. (2018); FeHx : Shahr et al. (2016).
 671

672 5. Conclusion

673 We have investigated the effects of site occupancies, chemical composition, spin
 674 transition, and valence state on the reduced Fe partition function ratio (β -factor) of $(\text{Mg},$
 675 $\text{Fe}^{2+}, \text{Fe}^{3+}, \text{Al}^{3+})(\text{Fe}^{3+}, \text{Al}^{3+}, \text{Si})\text{O}_3$ Bdg under lower-mantle pressure-temperature
 676 conditions by performing first-principles calculations and synergistic nuclear resonant
 677 inelastic X-ray scattering measurements. The computational partial phonon density of
 678 states of Fe^{3+} in $(\text{Mg}_{0.5}\text{Fe}^{3+}_{0.5})(\text{Si}_{0.5}\text{Fe}^{3+}_{0.5})\text{O}_3$ bridgmanite agree well with experimental
 679 measurements at high pressures. Our results reveal that Fe^{2+} -bearing Bdg has the
 680 smallest β -factor relative to other Fe^{3+} -bearing species. Site occupancies for Fe^{3+} can

681 have a significant effect on the β -factor of Bdg. Compared to the A-site HS Fe³⁺, the B-
682 site HS Fe³⁺ has a higher β -factor by $\sim 0.17\%$ at 40 GPa and 1000 K. The spin transition
683 of B-site Fe³⁺ in Bdg influences its β -factor more significantly than variations in valence
684 state and chemical composition, with an increase of $\sim +0.83\%$ across the spin transition
685 at 1000 K. This change would be diminished to $+0.09\%$ along an expected geotherm
686 of the lower mantle. The variation of β -factors is mainly controlled by the Fe-O bond
687 lengths, and the shorter bond lengths correspond to higher bond strength and β -factors.
688 In addition, although the incorporation of Al³⁺ into the Bdg B-site results in a mild
689 effect on the β -factor of A-site Fe³⁺ when compared to (Mg_{0.5}Fe³⁺_{0.5})(Si_{10.5}Fe³⁺_{0.5})O₃
690 Bdg, the presence of Al in Earth's lower mantle would decrease the impact of B-site
691 Fe³⁺ spin transition on the β -factor of Bdg by preventing Fe³⁺ from occupying the B-
692 site. Combined with previous data, our models demonstrate that Fe isotopic
693 fractionation between Fp and Bdg in most parts of the lower mantle would not be
694 significant, except the lowermost parts. The crystallization of the magma ocean is also
695 unlikely to have resulted in significant iron isotopic fractionation in any deep-mantle
696 reservoir. In contrast, under the conditions of the core-mantle boundary, low-spin Fe-
697 bearing mantle minerals could concentrate heavy Fe isotopes by up to $+0.20\%$ through
698 core-mantle interaction.

699

700 **Acknowledgements**

701 W.Z. Wang and Z.Q. Wu acknowledge the Strategic Priority Research Program of
702 the Chinese Academy of Sciences (XDB18000000), the Natural Science Foundation of
703 China (41721002, 41925017). J.F.L. acknowledges support from the Geophysics
704 Program of the National Science Foundation (EAR-1502594). S.M.D. also
705 acknowledges support from NSF CSEDI (EAR-1664332). NRIXS experiments used
706 resources of the Advanced Photon Source, a U.S. Department of Energy (DOE) Office
707 of Science User Facility operated for the DOE Office of Science by Argonne National
708 Laboratory under Contract No. DE-AC02-06CH11357. We are grateful to the
709 constructive comments from Paolo Sossi and the other two anonymous reviewers and
710 editorial handling by Mike Toplis and Jeffrey G. Catalano.

711

712 **Research Data**

713 Relevant data is provided in Electronic Supplementary materials.

714 **References**

- 715 Akahama Y. and Kawamura H. (2010) Pressure calibration of diamond anvil Raman
716 gauge to 410 GPa. *J. Phys. Conf. Ser.* **215**, 012195. Available at:
717 [http://stacks.iop.org/1742-](http://stacks.iop.org/1742-6596/215/i=1/a=012195?key=crossref.e13853a2cfe73464df62698f42525ac4)
718 [6596/215/i=1/a=012195?key=crossref.e13853a2cfe73464df62698f42525ac4](http://stacks.iop.org/1742-6596/215/i=1/a=012195?key=crossref.e13853a2cfe73464df62698f42525ac4).
- 719 Andrault D., Muñoz M., Pesce G., Cerantola V., Chumakov A., Kantor I., Pascarelli
720 S., Rüffer R. and Hennet L. (2018) Large oxygen excess in the primitive mantle
721 could be the source of the Great Oxygenation Event. *Geochemical Perspect.*
722 *Lett.*, 5–10. Available at:
723 <http://www.geochemicalperspectivesletters.org/article1801>.
- 724 Anisimov V. I., Zaanen J. and Andersen O. K. (1991) Band theory and Mott
725 insulators: Hubbard U instead of Stoner I. *Phys. Rev. B* **44**, 943–954.
- 726 Armstrong K., Frost D. J., McCammon C. A., Rubie D. C. and Boffa Ballaran T.
727 (2019) Deep magma ocean formation set the oxidation state of Earth's mantle.
728 *Science (80-.)*. **365**, 903–906.
- 729 Bigeleisen J. and Mayer M. G. (1947) Calculation of Equilibrium Constants for
730 Isotopic Exchange Reactions. *J. Chem. Phys.* **15**, 261. Available at:
731 <http://scitation.aip.org/content/aip/journal/jcp/15/5/10.1063/1.1746492>.
- 732 Blanchard M., Dauphas N., Hu M. Y., Roskosz M., Alp E. E., Golden D. C., Sio C.
733 K., Tissot F. L. H., Zhao J., Gao L., Morris R. V., Fornace M., Floris A., Lazzeri
734 M. and Balan E. (2015) Reduced partition function ratios of iron and oxygen in
735 goethite. *Geochim. Cosmochim. Acta* **151**, 19–33. Available at:
736 <https://linkinghub.elsevier.com/retrieve/pii/S0016703714007157>.
- 737 Boukaré C.-E., Ricard Y. and Fiquet G. (2015) Thermodynamics of the MgO-FeO-
738 SiO₂ system up to 140 GPa: Application to the crystallization of Earth's magma
739 ocean. *J. Geophys. Res. Solid Earth* **120**, 6085–6101. Available at:
740 <http://doi.wiley.com/10.1002/2015JB011929>.
- 741 Brown J. M. and McQueen R. G. (1986) Phase transitions, Grüneisen parameter, and
742 elasticity for shocked iron between 77 GPa and 400 GPa. *J. Geophys. Res. Solid*
743 *Earth* **91**, 7485–7494. Available at:
744 <http://doi.wiley.com/10.1029/JB091iB07p07485>.
- 745 CANIL D. and O'NEILL H. S. C. (1996) Distribution of Ferric Iron in some Upper-
746 Mantle Assemblages. *J. Petrol.* **37**, 609–635. Available at:
747 [https://academic.oup.com/petrology/article-](https://academic.oup.com/petrology/article-lookup/doi/10.1093/petrology/37.3.609)
748 [lookup/doi/10.1093/petrology/37.3.609](https://academic.oup.com/petrology/article-lookup/doi/10.1093/petrology/37.3.609).
- 749 Catalli K., Shim S. H., Prakapenka V. B., Zhao J. and Sturhahn W. (2010) X-ray
750 diffraction and Mössbauer spectroscopy of Fe³⁺- bearing Mg-silicate post-
751 perovskite at 128-138 GPa. *Am. Mineral.* **95**, 418–421.
- 752 Catalli Krystle, Shim S. H., Prakapenka V. B., Zhao J., Sturhahn W., Chow P., Xiao
753 Y., Liu H., Cynn H. and Evans W. J. (2010) Spin state of ferric iron in MgSiO₃
754 perovskite and its effect on elastic properties. *Earth Planet. Sci. Lett.* **289**, 68–75.
755 Available at: <http://dx.doi.org/10.1016/j.epsl.2009.10.029>.

756 Chen B., Lai X., Li J., Liu J., Zhao J., Bi W., Ercan Alp E., Hu M. Y. and Xiao Y.
757 (2018) Experimental constraints on the sound velocities of cementite Fe₃C to
758 core pressures. *Earth Planet. Sci. Lett.* **494**, 164–171. Available at:
759 <https://doi.org/10.1016/j.epsl.2018.05.002>.

760 Chen B., Li Z., Zhang D., Liu J., Hu M. Y., Zhao J., Bi W., Alp E. E., Xiao Y., Chow
761 P. and Li J. (2014) Hidden carbon in Earth's inner core revealed by shear
762 softening in dense Fe₇C₃. *Proc. Natl. Acad. Sci.* **111**, 17755–17758. Available
763 at: <http://www.pnas.org/lookup/doi/10.1073/pnas.1411154111>.

764 Cococcioni M. and de Gironcoli S. (2005) Linear response approach to the calculation
765 of the effective interaction parameters in the LDA+U method. *Phys. Rev. B* **71**,
766 035105. Available at:
767 <http://link.aps.org/doi/10.1103/PhysRevB.71.035105>
768 <http://arxiv.org/abs/cond-mat/0405160>.

769 Craddock P. R. and Dauphas N. (2011) Iron Isotopic Compositions of Geological
770 Reference Materials and Chondrites. *Geostand. Geoanalytical Res.* **35**, 101–123.
771 Available at: <http://doi.wiley.com/10.1111/j.1751-908X.2010.00085.x>.

772 Craddock P. R., Warren J. M. and Dauphas N. (2013) Abyssal peridotites reveal the
773 near-chondritic Fe isotopic composition of the Earth. *Earth Planet. Sci. Lett.* **365**,
774 63–76. Available at: <http://dx.doi.org/10.1016/j.epsl.2013.01.011>.

775 Dauphas N., Hu M. Y., Baker E. M., Hu J., Tissot F. L. H., Alp E. E., Roskosz M.,
776 Zhao J., Bi W., Liu J., Lin J.-F., Nie N. X. and Heard A. (2018) SciPhon: a data
777 analysis software for nuclear resonant inelastic X-ray scattering with applications
778 to Fe, Kr, Sn, Eu and Dy. *J. Synchrotron Radiat.* **25**, 1581–1599.

779 Dauphas N., Roskosz M., Alp E. E., Golden D. C., Sio C. K., Tissot F. L. H., Hu M.
780 Y., Zhao J., Gao L. and Morris R. V. (2012) A general moment NRIXS approach
781 to the determination of equilibrium Fe isotopic fractionation factors: Application
782 to goethite and jarosite. *Geochim. Cosmochim. Acta* **94**, 254–275. Available at:
783 <http://linkinghub.elsevier.com/retrieve/pii/S0016703712003663>.

784 Dauphas N., Roskosz M., Alp E. E., Neuville D. R., Hu M. Y., Sio C. K., Tissot F. L.
785 H., Zhao J., Tissandier L., Médard E. and Cordier C. (2014) Magma redox and
786 structural controls on iron isotope variations in Earth's mantle and crust. *Earth
787 Planet. Sci. Lett.* **398**, 127–140.

788 Dorfman S. M., Potapkin V., Lv M., Greenberg E., Kuppenko I., Chumakov A. I., Bi
789 W., Alp E. E., Liu J., Magrez A., Dutton S. E., Cava R. J., McCammon C. A. and
790 Gillet P. (2020) Effects of composition and pressure on electronic states of iron
791 in bridgmanite. *Am. Mineral.* **105**, 1030–1039. Available at:
792 [https://pubs.geoscienceworld.org/msa/ammin/article/105/7/1030/587519/Effects-
793 of-composition-and-pressure-on-electronic](https://pubs.geoscienceworld.org/msa/ammin/article/105/7/1030/587519/Effects-of-composition-and-pressure-on-electronic).

794 Elardo S. M. and Shahar A. (2017) Non-chondritic iron isotope ratios in planetary
795 mantles as a result of core formation. *Nat. Geosci.* **10**, 317–321.

796 Feng C., Qin T., Huang S., Wu Z. and Huang F. (2014) First-principles investigations
797 of equilibrium calcium isotope fractionation between clinopyroxene and Ca-

798 doped orthopyroxene. *Geochim. Cosmochim. Acta* **143**, 132–142. Available at:
799 <http://dx.doi.org/10.1016/j.gca.2014.06.002>.

800 Fischer R. A., Nakajima Y., Campbell A. J., Frost D. J., Harries D., Langenhorst F.,
801 Miyajima N., Pollok K. and Rubie D. C. (2015) High pressure metal–silicate
802 partitioning of Ni, Co, V, Cr, Si, and O. *Geochim. Cosmochim. Acta* **167**, 177–
803 194. Available at:
804 <https://linkinghub.elsevier.com/retrieve/pii/S0016703715004093>.

805 Frost D. J., Liebske C., Langenhorst F., McCammon C. a, Tronnes R. G. and Rubie
806 D. C. (2004) Experimental evidence for the existence of iron-rich metal in the
807 Earth’ s lower mantle. *Nature* **428**, 409–412.

808 Frost D. J. and McCammon C. A. (2008) The Redox State of Earth’s Mantle. *Annu.*
809 *Rev. Earth Planet. Sci.* **36**, 389–420. Available at:
810 <http://www.annualreviews.org/doi/10.1146/annurev.earth.36.031207.124322>.

811 Fu S., Yang J., Zhang Y., Liu J., Greenberg E., Prakapenka V. B., Okuchi T. and Lin
812 J. F. (2018a) Melting behavior of the lower-mantle ferropericlase across the spin
813 crossover: Implication for the ultra-low velocity zones at the lowermost mantle.
814 *Earth Planet. Sci. Lett.* **503**, 1–9. Available at:
815 <https://doi.org/10.1016/j.epsl.2018.09.014>.

816 Fu S., Yang J., Zhang Y., Okuchi T., McCammon C., Kim H. I., Lee S. K. and Lin J.
817 F. (2018b) Abnormal Elasticity of Fe-Bearing Bridgmanite in the Earth’s Lower
818 Mantle. *Geophys. Res. Lett.* **45**, 4725–4732.

819 Giannozzi P., Baroni S., Bonini N., Calandra M., Car R., Cavazzoni C., Ceresoli D.,
820 Chiarotti G. L., Cococcioni M., Dabo I., Dal Corso A., de Gironcoli S., Fabris S.,
821 Fratesi G., Gebauer R., Gerstmann U., Gougoussis C., Kokalj A., Lazzeri M.,
822 Martin-Samos L., Marzari N., Mauri F., Mazzarello R., Paolini S., Pasquarello
823 A., Paulatto L., Sbraccia C., Scandolo S., Sclauzero G., Seitsonen A. P.,
824 Smogunov A., Umari P. and Wentzcovitch R. M. (2009) QUANTUM
825 ESPRESSO: a modular and open-source software project for quantum
826 simulations of materials. *J. Phys. Condens. Matter* **21**, 395502. Available at:
827 [http://stacks.iop.org/0953-](http://stacks.iop.org/0953-8984/21/i=39/a=395502?key=crossref.c21336c286fa6d3db893262ae3f6e151)
828 [8984/21/i=39/a=395502?key=crossref.c21336c286fa6d3db893262ae3f6e151](http://stacks.iop.org/0953-8984/21/i=39/a=395502?key=crossref.c21336c286fa6d3db893262ae3f6e151).

829 Hsu H., Blaha P., Cococcioni M. and Wentzcovitch R. M. (2011) Spin-State
830 Crossover and Hyperfine Interactions of Ferric Iron in MgSiO₃ Perovskite. *Phys.*
831 *Rev. Lett.* **106**, 118501. Available at:
832 <https://link.aps.org/doi/10.1103/PhysRevLett.106.118501>.

833 Hsu H., Umemoto K., Blaha P. and Wentzcovitch R. M. (2010) Spin states and
834 hyperfine interactions of iron in (Mg,Fe)SiO₃ perovskite under pressure. *Earth*
835 *Planet. Sci. Lett.* **294**, 19–26. Available at:
836 <https://linkinghub.elsevier.com/retrieve/pii/S0012821X10001330>.

837 Huang F., Chen L., Wu Z. and Wang W. (2013) First-principles calculations of
838 equilibrium Mg isotope fractionations between garnet, clinopyroxene,
839 orthopyroxene, and olivine: Implications for Mg isotope thermometry. *Earth*

840 *Planet. Sci. Lett.* **367**, 61–70. Available at:
841 <http://dx.doi.org/10.1016/j.epsl.2013.02.025>.

842 Huang F., Wu Z., Huang S. and Wu F. (2014) First-principles calculations of
843 equilibrium silicon isotope fractionation among mantle minerals. *Geochim.*
844 *Cosmochim. Acta* **140**, 509–520. Available at:
845 <http://dx.doi.org/10.1016/j.gca.2014.05.035>.

846 Irifune T. and Ringwood A. E. (1987) Phase transformations in a harzburgite
847 composition to 26 GPa: implications for dynamical behaviour of the subducting
848 slab. *Earth Planet. Sci. Lett.* **86**, 365–376. Available at:
849 <https://linkinghub.elsevier.com/retrieve/pii/0012821X87902330>.

850 Irifune T., Shinmei T., McCammon C. A., Miyajima N., Rubie D. C. and Frost D. J.
851 (2010) Iron Partitioning and Density Changes of Pyrolite in Earth's Lower
852 Mantle. *Science (80-.)*. **327**, 193–195. Available at:
853 <http://www.sciencemag.org/lookup/doi/10.1126/science.1181443>.

854 Kowalski P. M., Wunder B. and Jahn S. (2013) Ab initio prediction of equilibrium
855 boron isotope fractionation between minerals and aqueous fluids at high P and T.
856 *Geochim. Cosmochim. Acta* **101**, 285–301. Available at:
857 <http://dx.doi.org/10.1016/j.gca.2012.10.007>.

858 Leshner C. E., Dannberg J., Barfod G. H., Bennett N. R., Glessner J. J. G., Lacks D. J.
859 and Brenan J. M. (2020) Iron isotope fractionation at the core–mantle boundary
860 by thermodiffusion. *Nat. Geosci.* **13**, 382–386. Available at:
861 <http://dx.doi.org/10.1038/s41561-020-0560-y>.

862 Li J. and Agee C. B. (1996) Geochemistry of mantle–core differentiation at high
863 pressure. *Nature* **381**, 686–689. Available at:
864 <http://www.nature.com/articles/381686a0>.

865 Li J., Sturhahn W., Jackson J. M., Struzhkin V. V., Lin J. F., Zhao J., Mao H. K. and
866 Shen G. (2006) Pressure effect on the electronic structure of iron in
867 (Mg,Fe)(Si,Al)O₃ perovskite: a combined synchrotron Mössbauer and X-ray
868 emission spectroscopy study up to 100 GPa. *Phys. Chem. Miner.* **33**, 575–585.
869 Available at: <http://link.springer.com/10.1007/s00269-006-0105-y>.

870 Lin J.-F., Speziale S., Mao Z. and Marquardt H. (2013) EFFECTS OF THE
871 ELECTRONIC SPIN TRANSITIONS OF IRON IN LOWER MANTLE
872 MINERALS: IMPLICATIONS FOR DEEP MANTLE GEOPHYSICS AND
873 GEOCHEMISTRY. *Rev. Geophys.* **51**, 244–275. Available at:
874 <http://doi.wiley.com/10.1002/rog.20010>.

875 Liu J., Dauphas N., Roskosz M., Hu M. Y., Yang H., Bi W., Zhao J., Alp E. E., Hu J.
876 Y. and Lin J. F. (2017) Iron isotopic fractionation between silicate mantle and
877 metallic core at high pressure. *Nat. Commun.* **8**, ncomms14377.

878 Liu J., Dorfman S. M., Zhu F., Li J., Wang Y., Zhang D., Xiao Y., Bi W. and Ercan
879 Alp E. (2018) Valence and spin states of iron are invisible in Earth's lower
880 mantle. *Nat. Commun.* **9**, 1–9. Available at: [http://dx.doi.org/10.1038/s41467-](http://dx.doi.org/10.1038/s41467-018-03671-5)
881 [018-03671-5](http://dx.doi.org/10.1038/s41467-018-03671-5).

- 882 Liu J., Mysen B., Fei Y. and Li J. (2015) Recoil-free fractions of iron in aluminous
883 bridgmanite from temperature-dependent Mössbauer spectra. *Am. Mineral.* **100**,
884 1978–1984. Available at: [https://pubs.geoscienceworld.org/ammin/article/100/8-](https://pubs.geoscienceworld.org/ammin/article/100/8-9/1978-1984/106340)
885 [9/1978-1984/106340](https://pubs.geoscienceworld.org/ammin/article/100/8-9/1978-1984/106340).
- 886 Mao H. K., Xu J. and Bell P. M. (1986) Calibration of the ruby pressure gauge to 800
887 kbar under quasi-hydrostatic conditions. *J. Geophys. Res.* **91**, 4673. Available at:
888 <http://doi.wiley.com/10.1029/JB091iB05p04673>.
- 889 Mao Z., Lin J.-F., Liu J. and Prakapenka V. B. (2011) Thermal equation of state of
890 lower-mantle ferropericase across the spin crossover. *Geophys. Res. Lett.* **38**,
891 n/a-n/a. Available at: <http://doi.wiley.com/10.1029/2011GL049915>.
- 892 Mao Z., Lin J. F., Yang J., Inoue T. and Prakapenka V. B. (2015) Effects of the Fe³⁺
893 spin transition on the equation of state of bridgmanite. *Geophys. Res. Lett.* **42**,
894 4335–4342.
- 895 Marquardt H., Speziale S., Reichmann H. J., Frost D. J., Schilling F. R. and Garnero
896 E. J. (2009) Elastic Shear Anisotropy of Ferropericase in Earth's Lower Mantle.
897 *Science (80-.)*. **324**, 224–226. Available at:
898 <http://www.sciencemag.org/cgi/doi/10.1126/science.1169365>.
- 899 McCammon C. (1997) Perovskite as a possible sink for ferric iron in the lower
900 mantle. *Nature* **387**, 694–696. Available at:
901 <http://www.nature.com/articles/42685>.
- 902 McDonough W. F. and Sun S. -s. (1995) The composition of the Earth. *Chem. Geol.*
903 **120**, 223–253. Available at:
904 <http://linkinghub.elsevier.com/retrieve/pii/0009254194001404>.
- 905 Núñez-Valdez M., Wu Z., Yu Y. G. and Wentzcovitch R. M. (2013) Thermal
906 elasticity of (Fe_x,Mg_{1-x})₂SiO₄ olivine and wadsleyite. *Geophys. Res. Lett.*
907 **40**, 290–294. Available at: <http://doi.wiley.com/10.1002/grl.50131>.
- 908 Núñez Valdez M., Wu Z., Yu Y. G., Revenaugh J. and Wentzcovitch R. M. (2012)
909 Thermoelastic properties of ringwoodite (Fe_x,Mg_{1-x})₂SiO₄: Its relationship to
910 the 520km seismic discontinuity. *Earth Planet. Sci. Lett.* **351–352**, 115–122.
- 911 Poitrasson F. (2007) Does planetary differentiation really fractionate iron isotopes?
912 *Earth Planet. Sci. Lett.* **256**, 484–492.
- 913 Poitrasson F., Delpech G. and Grégoire M. (2013) On the iron isotope heterogeneity
914 of lithospheric mantle xenoliths: implications for mantle metasomatism, the
915 origin of basalts and the iron isotope composition of the Earth. *Contrib. to*
916 *Mineral. Petrol.* **165**, 1243–1258. Available at:
917 <http://link.springer.com/10.1007/s00410-013-0856-7>.
- 918 Poitrasson F., Halliday A. N., Lee D. C., Levasseur S. and Teutsch N. (2004) Iron
919 isotope differences between Earth, Moon, Mars and Vesta as possible records of
920 contrasted accretion mechanisms. *Earth Planet. Sci. Lett.* **223**, 253–266.
- 921 Poitrasson F., Roskosz M. and Corgne A. (2009) No iron isotope fractionation
922 between molten alloys and silicate melt to 2000 °C and 7.7 GPa: Experimental
923 evidence and implications for planetary differentiation and accretion. *Earth*

924 *Planet. Sci. Lett.* **278**, 376–385. Available at:
925 <http://dx.doi.org/10.1016/j.epsl.2008.12.025>.

926 Polyakov V. B. (2009) Equilibrium Iron Isotope Fractionation at Core-Mantle
927 Boundary Conditions. *Science (80-.)*. **323**, 912–914. Available at:
928 <http://www.sciencemag.org/cgi/doi/10.1126/science.1166329>.

929 Qian W., Wang W., Zou F. and Wu Z. (2018) Elasticity of Orthoenstatite at High
930 Pressure and Temperature: Implications for the Origin of Low V P / V S Zones
931 in the Mantle Wedge. *Geophys. Res. Lett.* **45**, 665–673. Available at:
932 <http://doi.wiley.com/10.1002/2017GL075647>.

933 Rubie D. C., Nimmo F. and Melosh H. J. (2015) Formation of the Earth's Core. In
934 *Treatise on Geophysics* Elsevier. pp. 43–79. Available at:
935 <http://linkinghub.elsevier.com/retrieve/pii/B9780444538024001548>.

936 Rustad J. R. and Yin Q.-Z. (2009) Iron isotope fractionation in the Earth's lower
937 mantle. *Nat. Geosci.* **2**, 514–518. Available at:
938 <http://dx.doi.org/10.1038/ngeo546>.

939 Schauble E. A. (2011) First-principles estimates of equilibrium magnesium isotope
940 fractionation in silicate, oxide, carbonate and hexaaquamagnesium(2+) crystals.
941 *Geochim. Cosmochim. Acta* **75**, 844–869. Available at:
942 <http://linkinghub.elsevier.com/retrieve/pii/S0016703710006332>.

943 Shahar A., Schauble E. A., Caracas R., Gleason A. E., Reagan M. M., Xiao Y., Shu J.
944 and Mao W. (2016) Pressure-dependent isotopic composition of iron alloys.
945 *Science (80-.)*. **352**, 580–582.

946 Shim S.-H., Grocholski B., Ye Y., Alp E. E., Xu S., Morgan D., Meng Y. and
947 Prakapenka V. B. (2017) Stability of ferrous-iron-rich bridgmanite under
948 reducing midmantle conditions. *Proc. Natl. Acad. Sci.* **114**, 6468–6473.
949 Available at: <http://www.pnas.org/lookup/doi/10.1073/pnas.1614036114>.

950 Shukla G. and Wentzcovitch R. M. (2016) Spin crossover in
951 (Mg,Fe³⁺)(Si,Fe³⁺)O₃bridgmanite: Effects of disorder, iron concentration, and
952 temperature. *Phys. Earth Planet. Inter.* **260**, 53–61. Available at:
953 <http://dx.doi.org/10.1016/j.pepi.2016.09.003>.

954 Shukla G., Wu Z., Hsu H., Floris A., Cococcioni M. and Wentzcovitch R. M. (2015)
955 Thermoelasticity of Fe²⁺-bearing bridgmanite. *Geophys. Res. Lett.* **42**, 1741–
956 1749. Available at: <http://doi.wiley.com/10.1002/2014GL062888>.

957 Siebert J., Badro J., Antonangeli D. and Ryerson F. J. (2012) Metal-silicate
958 partitioning of Ni and Co in a deep magma ocean. *Earth Planet. Sci. Lett.* **321–**
959 **322**, 189–197. Available at: <http://dx.doi.org/10.1016/j.epsl.2012.01.013>.

960 Sossi P. A., Halverson G. P., Nebel O. and Eggins S. M. (2015) Combined Separation
961 of Cu, Fe and Zn from Rock Matrices and Improved Analytical Protocols for
962 Stable Isotope Determination. *Geostand. Geoanalytical Res.* **39**, 129–149.
963 Available at: <http://doi.wiley.com/10.1111/j.1751-908X.2014.00298.x>.

964 Sossi P. A., Nebel O. and Foden J. (2016) Iron isotope systematics in planetary
965 reservoirs. *Earth Planet. Sci. Lett.* **452**, 295–308. Available at:

966 <http://dx.doi.org/10.1016/j.epsl.2016.07.032>.

967 Teng F.-Z., Dauphas N. and Helz R. T. (2008) Iron Isotope Fractionation During
968 Magmatic Differentiation in Kilauea Iki Lava Lake. *Science* (80-). **320**, 1620–
969 1622. Available at:
970 <http://www.sciencemag.org/cgi/doi/10.1126/science.1157166>.

971 Teng F.-Z., Dauphas N. and Watkins J. M. (2017) Non-Traditional Stable Isotopes:
972 Retrospective and Prospective. *Rev. Mineral. Geochemistry* **82**, 1 LP – 26.
973 Available at: <http://ring.geoscienceworld.org/content/82/1/1.abstract>.

974 Teng F. Z., Dauphas N., Huang S. and Marty B. (2013) Iron isotopic systematics of
975 oceanic basalts. *Geochim. Cosmochim. Acta* **107**, 12–26. Available at:
976 <http://dx.doi.org/10.1016/j.gca.2012.12.027>.

977 Togo A. and Tanaka I. (2015) First principles phonon calculations in materials
978 science. *Scr. Mater.* **108**, 1–5. Available at:
979 <http://dx.doi.org/10.1016/j.scriptamat.2015.07.021>.

980 Vanderbilt D. (1990) Soft self-consistent pseudopotentials in a generalized eigenvalue
981 formalism. *Phys. Rev. B* **41**, 7892–7895. Available at:
982 <http://link.aps.org/doi/10.1103/PhysRevB.41.7892>.

983 Wang W., Qin T., Zhou C., Huang S., Wu Z. and Huang F. (2017a) Concentration
984 effect on equilibrium fractionation of Mg-Ca isotopes in carbonate minerals:
985 Insights from first-principles calculations. *Geochim. Cosmochim. Acta* **208**, 185–
986 197. Available at: <http://dx.doi.org/10.1016/j.gca.2017.03.023>.

987 Wang W., Walter M. J., Peng Y., Redfern S. and Wu Z. (2019a) Constraining olivine
988 abundance and water content of the mantle at the 410-km discontinuity from the
989 elasticity of olivine and wadsleyite. *Earth Planet. Sci. Lett.* **519**, 1–11. Available
990 at: <https://doi.org/10.1016/j.epsl.2019.04.018>.

991 Wang W. and Wu Z. (2018) Elasticity of Corundum at High Pressures and
992 Temperatures: Implications for Pyrope Decomposition and Al-Content Effect on
993 Elastic Properties of Bridgmanite. *J. Geophys. Res. Solid Earth* **123**, 1201–1216.
994 Available at: <http://doi.wiley.com/10.1002/2017JB015088>.

995 Wang W., Zhou C., Liu Y., Wu Z. and Huang F. (2019b) Equilibrium Mg isotope
996 fractionation among aqueous Mg²⁺, carbonates, brucite and lizardite: Insights
997 from first-principles molecular dynamics simulations. *Geochim. Cosmochim.*
998 *Acta* **250**, 117–129. Available at: <https://doi.org/10.1016/j.gca.2019.01.042>.

999 Wang W., Zhou C., Qin T., Kang J., Huang S., Wu Z. and Huang F. (2017b) Effect of
1000 Ca content on equilibrium Ca isotope fractionation between orthopyroxene and
1001 clinopyroxene. *Geochim. Cosmochim. Acta* **219**, 44–56. Available at:
1002 <http://dx.doi.org/10.1016/j.gca.2017.09.022>.

1003 Wang X., Tsuchiya T. and Hase A. (2015) Computational support for a pyrolytic
1004 lower mantle containing ferric iron. *Nat. Geosci.* **8**, 556–559. Available at:
1005 <http://www.nature.com/doi/10.1038/ngeo2458>.

1006 Wicks J. K., Jackson J. M. and Sturhahn W. (2010) Very low sound velocities in iron-
1007 rich (Mg,Fe)O: Implications for the core-mantle boundary region. *Geophys. Res.*

1008 *Lett.* **37**, n/a-n/a. Available at: <http://doi.wiley.com/10.1029/2010GL043689>.

1009 Woodland A. B., Kornprobst J. and Tabit A. (2006) Ferric iron in orogenic lherzolite
1010 massifs and controls of oxygen fugacity in the upper mantle. *Lithos* **89**, 222–241.

1011 Wu Z. (2016) Velocity structure and composition of the lower mantle with spin
1012 crossover in ferropericlase. *J. Geophys. Res. Solid Earth* **121**, 2304–2314.
1013 Available at: <http://doi.wiley.com/10.1002/2015JB012667>.

1014 Wu Z., Huang F. and Huang S. (2015a) Isotope fractionation induced by phase
1015 transformation: First-principles investigation for Mg₂SiO₄. *Earth Planet. Sci.*
1016 *Lett.* **409**, 339–347. Available at: <http://dx.doi.org/10.1016/j.epsl.2014.11.004>.

1017 Wu Z., Huang F. and Huang S. (2015b) Isotope fractionation induced by phase
1018 transformation: First-principles investigation for Mg₂SiO₄. *Earth Planet. Sci.*
1019 *Lett.* **409**, 339–347.

1020 Wu Z., Justo J. F. and Wentzcovitch R. M. (2013) Elastic Anomalies in a Spin-
1021 Crossover System: Ferropericlase at Lower Mantle Conditions. *Phys. Rev. Lett.*
1022 **110**, 228501. Available at:
1023 <http://link.aps.org/doi/10.1103/PhysRevLett.110.228501>.

1024 Yang H., Lin J. F., Hu M. Y., Roskosz M., Bi W., Zhao J., Alp E. E., Liu Jin, Liu
1025 Jiachao, Wentzowitch R. M., Okuchi T. and Dauphas N. (2019) Iron isotopic
1026 fractionation in mineral phases from Earth's lower mantle: Did terrestrial magma
1027 ocean crystallization fractionate iron isotopes? *Earth Planet. Sci. Lett.* **506**, 113–
1028 122. Available at: <https://doi.org/10.1016/j.epsl.2018.10.034>.

1029 Yu Y. G., Hsu H., Cococcioni M. and Wentzcovitch R. M. (2012) Spin states and
1030 hyperfine interactions of iron incorporated in MgSiO₃post-perovskite. *Earth*
1031 *Planet. Sci. Lett.* **331–332**, 1–7.

1032 Zhang S., Cottaar S., Liu T., Stackhouse S. and Militzer B. (2016) High-pressure,
1033 temperature elasticity of Fe- and Al-bearing MgSiO₃: Implications for the
1034 Earth's lower mantle. *Earth Planet. Sci. Lett.* **434**, 264–273. Available at:
1035 <http://dx.doi.org/10.1016/j.epsl.2015.11.030>.

1036